

RESEARCH ARTICLE

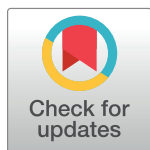
# Comparing individual-based approaches to modelling the self-organization of multicellular tissues

James M. Osborne<sup>1</sup>\*, Alexander G. Fletcher<sup>2,3</sup>\*, Joe M. Pitt-Francis<sup>4</sup>, Philip K. Maini<sup>5</sup>, David J. Gavaghan<sup>4</sup>

**1** School of Mathematics and Statistics, University of Melbourne, Parkville, Victoria, Australia, **2** School of Mathematics and Statistics, University of Sheffield, Sheffield, United Kingdom, **3** Bateson Centre, University of Sheffield, Sheffield, United Kingdom, **4** Department of Computer Science, University of Oxford, Oxford, United Kingdom, **5** Wolfson Centre for Mathematical Biology, Mathematical Institute, University of Oxford, Oxford, United Kingdom

✉ These authors contributed equally to this work.

\* [jmosborne@unimelb.edu.au](mailto:jmosborne@unimelb.edu.au) (JMO); [a.g.fletcher@sheffield.ac.uk](mailto:a.g.fletcher@sheffield.ac.uk) (AGF)



## Abstract

### OPEN ACCESS

**Citation:** Osborne JM, Fletcher AG, Pitt-Francis JM, Maini PK, Gavaghan DJ (2017) Comparing individual-based approaches to modelling the self-organization of multicellular tissues. PLoS Comput Biol 13(2): e1005387. doi:10.1371/journal.pcbi.1005387

**Editor:** Qing Nie, University of California Irvine, UNITED STATES

**Received:** September 18, 2016

**Accepted:** January 28, 2017

**Published:** February 13, 2017

**Copyright:** © 2017 Osborne et al. This is an open access article distributed under the terms of the [Creative Commons Attribution License](#), which permits unrestricted use, distribution, and reproduction in any medium, provided the original author and source are credited.

**Data Availability Statement:** All relevant data are within the paper and its Supporting Information files.

**Funding:** JMO and AGF acknowledge funding from the Engineering and Physical Sciences Research Council (EPSRC <https://www.epsrc.ac.uk/>) through grant EP/I017909/1 awarded to PKM and DJG. JMO, AGF and JMF acknowledge funding from the Biotechnology and Biological Sciences Research Council (BBSRC <http://www.bbsrc.ac.uk/>) through grant BB/D020190/1 awarded to PKM

The coordinated behaviour of populations of cells plays a central role in tissue growth and renewal. Cells react to their microenvironment by modulating processes such as movement, growth and proliferation, and signalling. Alongside experimental studies, computational models offer a useful means by which to investigate these processes. To this end a variety of cell-based modelling approaches have been developed, ranging from lattice-based cellular automata to lattice-free models that treat cells as point-like particles or extended shapes. However, it remains unclear how these approaches compare when applied to the same biological problem, and what differences in behaviour are due to different model assumptions and abstractions. Here, we exploit the availability of an implementation of five popular cell-based modelling approaches within a consistent computational framework, Chaste (<http://www.cs.ox.ac.uk/chaste>). This framework allows one to easily change constitutive assumptions within these models. In each case we provide full details of all technical aspects of our model implementations. We compare model implementations using four case studies, chosen to reflect the key cellular processes of proliferation, adhesion, and short- and long-range signalling. These case studies demonstrate the applicability of each model and provide a guide for model usage.

## Author summary

In combination with molecular and live-imaging techniques, computational modelling plays an increasingly important role in the study of tissue growth and renewal. To this end a variety of cell-based modelling approaches have been developed, ranging in complexity from lattice-based cellular automata to lattice-free models that treat cells as point-like particles or extended shapes. However, it remains unclear how these approaches compare when applied to the same biological problem, and under which circumstances each

and DJG. The funders had no role in study design, data collection and analysis, decision to publish, or preparation of the manuscript.

**Competing interests:** The authors have declared that no competing interests exist.

approach is valid. Here we implement five classes of such model in a consistent computational framework, Chaste. We apply each model to four simulation studies, chosen to illustrate how the cellular processes such as proliferation, adhesion, and short- and long-range signalling may be implemented in each model. These case studies demonstrate the applicability of each model and highlight where one may expect to see qualitative differences between model behaviours. Taken together, these findings provide a guide for model usage.

## Introduction

Cells in eukaryotic organisms respond to physical and chemical cues through processes such as movement, growth, division, differentiation, death and secretion or surface presentation of signalling molecules. These processes must be tightly orchestrated to ensure correct tissue-level behaviour and their dysregulation lies at the heart of many diseases. The last decade has witnessed remarkable progress in molecular and live-imaging studies of the collective self-organization of cells in tissues. In combination with experimental studies, mathematical modelling is a useful tool with which to unravel the complex nonlinear interactions between processes at the subcellular, cellular and tissue scales from which organ- and organism-level function arises. The classical approach to modelling these processes treats the tissue as a continuum, using some form of homogenization argument to average over length scales much larger than the typical diameter of a cell. It can thus be difficult to incorporate heterogeneity between cells within a population, or investigate the effect of noise at various scales, within such models.

Facilitated by the reduction in cost of computing power, a number of discrete or ‘individual-based’ approaches have been developed to model the collective dynamics of multicellular tissues (Fig 1). Such models treat cells, or subcellular components, as discrete entities and provide natural candidates for studying the regulation of cell-level processes in tissue dynamics. However, they are less amenable to mathematical analysis than their continuum counterparts. The precise rules and methods of implementation differ between models and must be adapted to a particular biological system. However, they can be broadly categorised as on- and off-lattice, according to whether or not cells are constrained to lie on an artificial lattice. In the present work, we choose to focus on five of the most widely used approaches. Each of the models described below have been helpful in furthering our knowledge but, like all models, they are simplifications and so have limitations.

Arguably the simplest individual-based models are cellular automata (CA), where each lattice site can contain at most a single cell (Fig 1(a)). The system is evolved discretely, using a fixed time-stepping [1] or event-driven [2] approach, with the new state of each cell determined using deterministic or stochastic rules and the state of the system at the previous time step. The computational simplicity of CA renders them amenable to simulating large numbers of cells.

Another class of on-lattice model is the cellular Potts (CP) model [3], which represents each cell by several lattice sites, allowing for more realistic cell shapes (Fig 1(b)). The shape of each cell is evolved via some form of energy minimization. Unlike CA, the CP model can incorporate mechanical processes such as cell membrane tension, cell-cell and cell-substrate adhesion, and cell volume conservation. The CP model has been used to study biological processes ranging from cell sorting [4] and morphogenesis [5] to tumour growth [6].

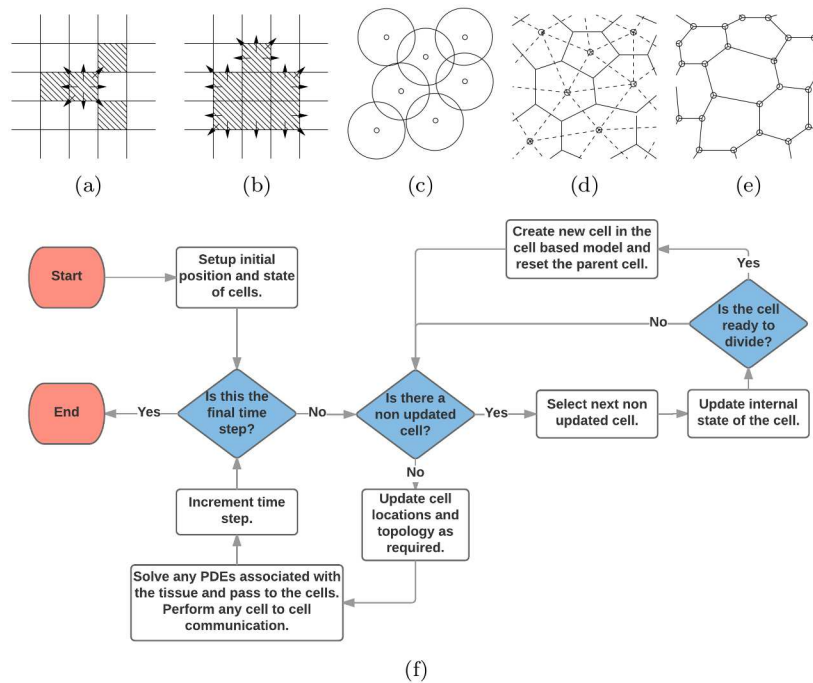


**Fig 1. Schematics of the cell-based models considered in this study.** (a) Cellular automaton (CA). (b) Cellular Potts (CP) model. (c) Overlapping spheres (OS) model. (d) Voronoi tessellation (VT) model. (e) Vertex model (VM). (f) Flow chart of cell-based simulation algorithm. See text for full details.

doi:10.1371/journal.pcbi.1005387.g001

The removal of a fixed-lattice geometry in off-lattice models enables the more detailed study of mechanical effects on cell populations. Two common descriptions of cell shape in off-lattice models are (i) ‘overlapping spheres’ (OS) or quasi-spherical particles [7] and (ii) through Voronoi tessellations (VT) [8]; in both approaches, the centre of each cell is tracked over time. In the former, cells are viewed as particles that are spherical in the absence of any interactions but which deform upon cell-cell or cell-substrate contact (Fig 1(c)). In the latter, the shape of each cell is defined to be the set of points in space that are nearer to the centre of the cell than the centres of any other cell; a Delaunay triangulation is performed to connect those cell centres that share a common face, thus determining the neighbours of each cell [9] (Fig 1(d)). In either case, Monte Carlo methods or Langevin equations may be used to simulate cell dynamics.

An alternative off-lattice approach commonly used to describe tightly packed epithelial cell sheets is the vertex model (VM) framework, in which each cell is modelled as a polygon, representing the cell’s membrane (Fig 1(e)). Each cell vertex, instead of centre, moves according to a balance of forces due to limited compressibility, cytoskeletal contractility and cell-cell adhesion. Additional rules govern cell neighbour rearrangements, growth, mitosis and death.

For the remainder of this work, we focus on the five classes of model outlined above; however, we note that a variety of other cell-based models have been developed, and are reviewed in detail elsewhere [10], [11], [12]. These include (among others) the finite element method [13], immersed boundary method [14] and subcellular element method [15].

A key advantage of cell-based models is that they can be straightforwardly coupled to other continuous models [16]. Several cell-based models have coupled descriptions of nutrient or morphogen transport and signalling to cell behaviour [17], [18], [19], [20], [21]. For example, a hybrid CA was used by Anderson and colleagues to study the role of the microenvironment

on solid tumour growth and response to therapy [22], while Aegerter-Wilmsen et al. coupled a vertex model of cell proliferation and rearrangement with a differential algebraic equation model for a protein regulatory network to describe the interplay between mechanics and signalling in regulating tissue size in the *Drosophila* wing imaginal disk [17].

As the use of cell-based models becomes increasingly widespread in the scientific community, it becomes ever more useful to be able to compare competing models within a consistent computational framework, to avoid the potential danger of artifacts associated with different methods of numerical solution. To date there has not been a comparison of the classes of models described above, due in part to the lack of a common computational framework in which to carry out such a comparison. The development of Chaste, an open-source C++ library for cell-based and multiscale modelling [23], [24], addresses this issue.

Here we present a systematic comparison of five classes of cell-based models through the use of four case studies. We demonstrate how the key cellular processes of proliferation, adhesion, and short- and long-range signalling can be implemented and compared within the competing modelling frameworks. Moreover, we provide a guide for which model is appropriate when representing a given system. We concentrate throughout on the two-dimensional case, but note that many of these models have also been implemented in three dimensions.

The remainder of this paper is structured as follows. We begin by presenting the five mathematical frameworks and discuss their implementation. Next, we use our four case studies to demonstrate how the modelling frameworks compare. Finally, we discuss our results and present a guide to which framework to use when modelling a particular problem.

## Materials and methods

In this study we compare the implementation and behaviour of: cellular automata (CA); cellular Potts (CP); cell-centre, both overlapping sphere (OS) and Voronoi tessellation (VT); and vertex (VM) models. We begin by briefly describing the governing rules and equations for each of these models focussing on the way they implement the common processes of cell-cell interaction and cell division. Throughout, full references are given to previous publications giving much fuller details of the derivation and implementation of each of these models. We also present a consistent numerical implementation for the models.

### Cellular automaton (CA) model

There are several possible ways to represent cell movement in a CA. Here we focus on compact tissues so consider movement driven by division and cell exchange, using a shoving-based approach [25]. The spatial domain is discretised into a regular lattice with cells occupying the individual lattice sites (Fig 1(a)). The area  $A_i$  of each cell  $i$  in this model is given by 1 squared cell diameter ( $CD^2$ ).

In common with all of the cell-based models presented here, cell proliferation is determined by a model of how cells progress through the cell cycle, which in turn specifies when cells divide. Our model of cell-cycle progression varies across the four examples considered. However, in all cases a dividing cell selects a random lattice site from its Moore neighbourhood (the eight cells that surround it), and all cells along the row, column or diagonal from the dividing cell's location are instantaneously displaced or 'shoved' to make space for the new cell.

We use a Metropolis-Hastings algorithm to make additional updates to the state of the tissue using asynchronous updating. At each time step  $\Delta t$ , after checking for and implementing any cell divisions, we sample with replacement  $N_{\text{Cells}}$  cells, where  $N_{\text{Cells}}$  is the number of cells in the tissue at time  $t$  (thus, it may be the case that a cell is sampled more than once in a time

step, while others are not sampled). This sweeping of the domain is also known as a Monte Carlo Step (MCS). We randomly select a neighbouring lattice site from each sampled cell's Moore neighbourhood for a potential swap. The swapping of cells is intended to model random motility and the affinity of cells to form and break connections with adjacent cells.

Assigning the MCS to a time step  $\Delta t$  allows us to parametrize the timescale of the switching process and relate this to cell division. A probability per hour is assigned for the cells (or empty lattice site, which we refer to as a void) to swap locations,  $p_{\text{swap}}$ , which is calculated as

$$p_{\text{swap}} = \kappa_{\text{swap}} \min(1, e^{-\Delta H/T}), \quad (1)$$

where  $\kappa_{\text{swap}}$  represents the rate of switching and  $T$  represents the background level of cell switching, modelling random cell fluctuations. If  $T = 0$  then only energetically favourable swaps happen, and we use this as the default value for our simulations; as  $T$  increases, more energetically unfavourable swaps occur. Finally,  $\Delta H = H_1 - H_0$  denotes the change in adhesive energy due to the swap, with  $H_0$  and  $H_1$  being the energy in the original and changed configurations respectively, which is defined to be the sum of the adhesion energy between lattice sites:

$$H = \sum_{(i,j) \in \mathcal{N}} \gamma(\tau(i), \tau(j)), \quad (2)$$

where  $\gamma(a, b)$  is a constant whose value depends on  $a$  and  $b$ , representing the adhesion energy between cells (or void) of type  $a$  and  $b$ ,  $\tau(k)$  is the type of cell  $k$  (or void if there is no cell on the lattice site) and  $\mathcal{N}$  is the set of all neighbouring lattice sites. Here  $\tau(k)$  takes the values 'A', 'B' and 'void', but can in principle be extended to more cell types. Note that while we have chosen the particular implementation of our CA to accommodate the case studies below, a variety of alternative implementations exist based on other updating schemes and cell division algorithms [26].

### Cellular Potts (CP) model

As in the CA, we discretize the spatial domain into a lattice. Although, as in the CA case, the structure and connectivity of this lattice may be arbitrary, for simplicity we restrict our attention to a regular square lattice of size  $N \times N$ . In contrast to the CA model, each cell is represented by a collection of lattice sites, with each site contained in at most one cell with the cell type of a lattice site being referred to as its spin. The area  $A_i$  of each cell  $i$  in this model is given by the sum of the area of all the lattice sites contained in the cell. In the present study, we represent a cell by 16 lattice sites (i.e. 1  $\text{CD}^2$  equals 16 lattice sites). This is illustrated in [Fig 1\(b\)](#).

In a similar manner to the CA, the system evolves by attempting to minimize a total 'energy' or Hamiltonian,  $H$ , over discrete time steps using a Metropolis-Hastings algorithm. The precise form of  $H$  varies across applications but can include contributions such as cell-cell adhesion, hydrostatic pressure, chemotaxis and haptotaxis [5]. One iteration of the algorithm consists of selecting a lattice site and a neighbouring site (from the Moore neighbourhood) at random and calculating the change in total energy resulting from copying the spin of the first site to the second,  $\Delta H = H_1 - H_0$ . The spin change is accepted with probability

$$p_{\text{copy}} = \min(1, e^{-\Delta H/T}), \quad (3)$$

where  $T$ , referred to as the 'temperature', characterizes fluctuations in the system; broadly speaking, at higher values of  $T$  cells move more freely, and hence system fluctuations increase in size. At each time step,  $\Delta t$ , we choose to sample with replacement  $N \times N$  lattice sites. Note that this established algorithm for simulating CP models permits cell fragmentation, in principle; however, recent work has overcome this limitation [27].

In this study, we use a Hamiltonian of the form

$$H = \sum_{i=1}^{N_{\text{Cells}}(t)} \left[ \alpha(A_i - A_i^{(0)})^2 + \beta(C_i - C_i^{(0)})^2 \right] + \sum_{(i,j) \in \mathcal{N}} (1 - \delta_{\sigma(i), \sigma(j)}) \gamma(\tau(i), \tau(j)), \quad (4)$$

where the first and second terms on the right-hand side represent the area and perimeter constraint energies, summed over each cell in the system, and the third term represents the adhesion energy. Here  $\sigma(k)$  denotes the index of the cell containing lattice site  $k$  (note we let  $\sigma(k) = 0$  if no cell is attached to the lattice site and we denote this to be the void), and  $\delta_{a,b}$  is the delta function, which equals 1 if  $a = b$  and 0 otherwise.  $\tau(k)$  denotes that cell's 'type' (with the type void if  $\sigma(k) = 0$ ), and  $\gamma$  denotes the interaction energies between cells occupying neighbouring lattice sites  $i$  and  $j$ . Again  $\mathcal{N}$  is the set of all neighbouring lattice sites and we allow  $\gamma$  to take different values for homotypic and heterotypic cell-cell interfaces and for 'boundary' interfaces between cells and the surrounding medium. Here  $A_k^{(0)}$  and  $C_k^{(0)}$  denote a specified 'target area' and 'target perimeter' for cell  $k$ , respectively, which can depend on internal properties of the cell, allowing for cell growth to be modelled. Here we assume all cells are mechanically identical and set  $A_k^{(0)} = A^{(0)}$  and  $C_k^{(0)} = C^{(0)}$ . The parameters  $\alpha$  and  $\beta$  influence how fast cells react to the area and perimeter constraints, respectively. Upon cell division, half the lattice sites are assigned to each daughter cell (with 2 cells of  $n + 1$  and  $n$  lattice sites, respectively, if the parent cell has  $2n + 1$  lattice sites).

## Cell-centre models

Here cells are represented by their centres, which are modelled as a set of points  $\{\mathbf{r}_1, \dots, \mathbf{r}_{N_{\text{Cells}}}\}$  which are free to move in space. For simplicity, we assume all cells to have identical mechanical properties and use force balance to derive the equations of motion. We balance forces on each cell centre and, making the standard assumption that inertial terms are small compared to dissipative terms (as cells move in dissipative environments of extremely small Reynolds number [28]), we obtain a first-order equation of motion for each cell centre,  $\mathbf{r}_i$ , given by

$$\eta \frac{d\mathbf{r}_i}{dt} = \mathbf{F}_i(t) = \sum_{j \in \mathcal{N}_i(t)} \mathbf{F}_{ij}(t), \quad (5)$$

where  $\eta$  denotes a damping constant and  $\mathbf{F}_i(t)$  is the total force acting on a cell  $i$  at time  $t$  which is assumed to equal the sum of all forces, coming from the connections with all neighbouring cells  $j \in \mathcal{N}_i(t)$  adjacent to  $i$  at that time,  $\mathbf{F}_{ij}(t)$ . The definition of  $\mathcal{N}_i(t)$  varies between the OS and VT models; in the former, it is the set of cells whose centres lie within a distance  $r_{\max}$  from the centre of cell  $i$ , while in the latter, it is the set of cells whose centres share an edge with the centre of cell  $i$  in the Delaunay triangulation. We solve this equation numerically using a simple forward Euler scheme with sufficiently small time step  $\Delta t$  to ensure numerical stability:

$$\mathbf{r}_i(t + \Delta t) = \mathbf{r}_i(t) + \frac{\Delta t}{\eta} \sum_{j \in \mathcal{N}_i(t)} \mathbf{F}_{ij}(t). \quad (6)$$

Upon cell division, we generate a random mitotic unit vector  $\hat{\mathbf{m}}$  and the daughter cells are placed at  $\mathbf{r}_i \pm \epsilon \hat{\mathbf{m}}$ , where  $\epsilon$  is a constant division separation parameter and is dependent on the particular cell-centre model being used.

**Overlapping spheres (OS).** Here, each cell  $i$  has an associated radius  $R_i$ . Two cells  $i$  and  $j$  are assumed to be neighbours if their centres satisfy  $\|\mathbf{r}_i - \mathbf{r}_j\| < r_{\max}$  for a fixed constant  $r_{\max}$  (where  $\|\cdot\|$  is the Euclidian norm) known as the interaction radius, where  $r_{\max} > 2R_i$  for all  $i$ . The area of the cell is defined as [29]

$$A_i = \pi(R_i^{\text{eff}})^2, \quad (7)$$

where

$$R_i^{\text{eff}} = \frac{1}{6} \left[ \sum_{j \in \mathcal{N}_i(t)} \frac{1}{2} (R_i - R_j + \|\mathbf{r}_{ij}\|) + R_i (6 - \text{size}(\mathcal{N}_i(t))) \right]. \quad (8)$$

Here  $\mathbf{r}_{ij}(t) = \mathbf{r}_j(t) - \mathbf{r}_i(t)$  is the vector from cell  $i$  to cell  $j$  at time  $t$ . An illustration of cell connectivity is given in [Fig 1\(d\)](#).

In the OS model we define the force between cells as [29]

$$\mathbf{F}_{ij}(t) = \begin{cases} \mu_{ij} s_{ij}(t) \hat{\mathbf{r}}_{ij}(t) \log \left( 1 + \frac{\|\mathbf{r}_{ij}(t)\| - s_{ij}(t)}{s_{ij}(t)} \right), & \text{for } \|\mathbf{r}_{ij}(t)\| < s_{ij}(t), \\ \mu_{ij} (\|\mathbf{r}_{ij}(t)\| - s_{ij}(t)) \hat{\mathbf{r}}_{ij}(t) \exp \left( -k_C \frac{\|\mathbf{r}_{ij}(t)\| - s_{ij}(t)}{s_{ij}(t)} \right), & \text{for } s_{ij}(t) \leq \|\mathbf{r}_{ij}(t)\| \leq r_{\max}, \\ 0, & \text{for } \|\mathbf{r}_{ij}(t)\| > r_{\max}. \end{cases} \quad (9)$$

Here  $\mu_{ij}$  is known as the “spring constant” and controls the size of the force (and depends on the cell types of the connected cells), by default  $\mu_{ij} = \mu$  for all interactions,  $\mathbf{r}_{ij}(t) = \mathbf{r}_j(t) - \mathbf{r}_i(t)$ ,  $\hat{\mathbf{r}}_{ij}(t)$  is the corresponding unit vector,  $k_C$  is a parameter which defines decay of the attractive force, and  $s_{ij}(t)$  is the natural separation between these two cells. For the OS model  $s_{ij}(t)$  is the sum of the radii of the two cells, and here the cell’s radius increases from 0.25 to 0.5 CDs over the first hour of the cell cycle, and hence is a function of time. Note that there is a cut-off distance,  $r_{\max}$ , such that once  $\|\mathbf{r}_{ij}(t)\| > r_{\max}$  the cells are not connected so the force is zero.

**Voronoi tessellation (VT).** In the VT model we represent cells by the Voronoi region of the cell centres (this is defined as the region of space that is nearer to one cell centre than any other). Example cell regions are shown as solid lines in [Fig 1\(d\)](#). In this model, the area  $A_i$  of a cell  $i$  is defined to be the area of the corresponding Voronoi region. Cell connectivity is defined by the dual of the Voronoi region, known as a Delaunay triangulation and this is shown by the dashed lines in [Fig 1\(d\)](#). Two cell centres are assumed to be connected if they share an edge in the Delaunay triangulation.

In the VT model we define the force between cells to be [8], [30],

$$\mathbf{F}_{ij}(t) = \mu_{ij} \hat{\mathbf{r}}_{ij}(t) \left( \|\mathbf{r}_{ij}(t)\| - s_{ij}(t) \right). \quad (10)$$

Here  $\mu_{ij}$  is the spring constant (defaulting to  $\mu_{ij} = \mu$ ),  $\mathbf{r}_{ij}(t) = \mathbf{r}_i(t) - \mathbf{r}_j(t)$ ,  $\hat{\mathbf{r}}_{ij}(t)$  is the corresponding unit vector and  $s_{ij}(t)$  is the natural separation between these two cells. For the VT model this increases linearly from  $s = \epsilon$  ( $= 0.1$ ) to  $s = 1$  over the first hour of the cell cycle.

When using a Delaunay triangulation to define cell connectivity, on a growing tissue, long edges can form between distant cells causing unrealistic connections to be made. There are two methods used to overcome this. The first is to introduce a cut-off length,  $r_{\max}$ , such that cells further apart than the cut-off length are no longer connected (analogous to the OS

model). The second method is to introduce *ghost nodes*, which are extra nodes introduced into the simulation which surround the tissue, which do not exert any forces on the cells, and preclude any long connections from forming. Moreover these ghost nodes ensure that the Voronoi regions, and therefore cell areas, are finite. In order for the ghost nodes to surround the tissue, as it grows, cells exert a force on the ghost nodes (and ghost nodes exert forces on other ghost nodes) causing them to move with the cells. The force applied is calculated using [Eq \(10\)](#). For more details on ghost nodes see [\[31\]](#).

### Vertex model (VM)

In the VM a tissue is represented by a collection of non-overlapping connected polygons whose vertices are free to move and each polygon corresponds to a cell. In this model, the area  $A_i$  of a cell  $i$  is given by the area of the associated polygon. An illustration of cells in a VM is given in [Fig 1\(e\)](#). As in cell-centre models we consider a set of points  $\{\mathbf{r}_1, \dots, \mathbf{r}_{N_{\text{Vertices}}}\}$ . Here we derive a force on each vertex from a phenomenological energy function, which we balance with a viscous drag term, leading to a first-order equation of motion (alternative formulations assume that the tissue evolves quasistatically [\[32\]](#), [\[33\]](#)):

$$\eta_V \frac{d\mathbf{r}_i}{dt} = -\nabla_i \left[ \sum_{j=1}^{N_{\text{Cells}}(t)} \left( \alpha (A_j - A_j^{(0)})^2 + \beta (C_j - C_j^{(0)})^2 \right) \right] - \nabla_i \left[ \sum_{j=1}^{N_{\text{Cells}}(t)} \left( \sum_{m=1}^{M_j} \gamma(\tau(j), \tau(j_m)) L_{j,m} \right) \right], \quad (11)$$

where  $\mathbf{r}_i$  is the position of vertex  $i$ ,  $\eta_V$  is an associated drag constant,  $\nabla_i$  is the gradient with respect to  $\mathbf{r}_i$  and  $N_{\text{Cells}}(t)$  denotes the number of cells in the system at time  $t$ . The variables  $A_j$  and  $C_j$  denote the area and the perimeter of cell  $j$ , respectively, and  $M_j$  is the number of vertices of cell  $j$ .  $L_{j,m}$  is the length of the line connecting vertices  $m$  and  $m + 1$  in cell  $j$  and  $j_m$  is the neighbour of cell  $j$  which shares the edge connecting vertices  $m$  and  $m + 1$  in cell  $j$ . Similar to the CP model,  $A^{(0)}$  is the cell's natural (or target) area, and  $C^{(0)}$  is its natural perimeter. Finally,  $\alpha$  and  $\beta$  are positive constants that represent a cell's resistance to changes in area or perimeter, respectively.  $\gamma$  again denotes the interaction energies between neighbouring cells. We allow  $\gamma$  to take different values for homotypic and heterotypic cell-cell interfaces and for 'boundary' interfaces between cells and the surrounding medium.

For simplicity here we set all cells to have a target area of  $A^{(0)} = 1$  and therefore a target perimeter of  $C^{(0)} = 2\sqrt{\pi}$ . See [\[34\]](#) for a discussion on the other growth options and their influence on simulations. Cell division is implemented by placing a new edge along the shortest axis through the dividing cell's centroid [\[35\]](#) and placing two new vertices at the intersection of this edge and the cell's perimeter, thus creating two daughter cells.

To maintain a non-overlapping tessellation of the domain we need to introduce a process where cell edges can swap, known as a T1 transition. This process allows cell connectivity to change as cells grow and move and is instrumental in the process of cell sorting. When an edge between two cells,  $A$  and  $B$ , becomes shorter than a given threshold,  $l_r$ , we rearrange the connectivity so that the cells  $A$  and  $B$  are no longer connected and the other cells that contain the vertices on the short edge,  $C$  and  $D$ , become connected. Other processes may also be required, such as a T2 transition where small triangular elements are removed to simulate cell death. For further details of these elementary operations, see [\[35\]](#).

As with all of these models, other force laws could be used to define cell interactions [\[36\]](#). For full details of the forces used in the vertex model, along with how they differ in both implementation and simulation results, see [\[35\]](#).

## Implementation

Now that we have briefly introduced all the cell-based models used in this study we proceed to discuss their implementation. Each simulation takes the form given in [Fig 1\(f\)](#). All components of this algorithm are the same for each simulation type except for the CA model where cells may also move due to the division of other cells. All models have been non-dimensiona-lised so that the units of space are cell diameters (CDs) and time is measured in hours.

Parameter values are, where possible, taken from published studies using the models. In these papers the parameters were identified by fitting global simulation behaviour to that of the biological system. Some parameters have been modified from their original values in order to make cell movement as similar as possible between models.

We implement all model simulations within Chaste, an open source C++ library that provides a systematic framework for multiscale multicellular simulations [24]. Further details on the implementation of VM and CP models within Chaste can be found in [35] and [37], respectively. All code used to generate the results presented in this paper, along with tutorials for running it, is released under an open source (BSD) license and is available at <https://chaste.cs.ox.ac.uk/trac/wiki/PaperTutorials/CellBasedComparison2017>.

## Results

We now present a series of case studies that illustrate how cellular processes can be represented in each cell-based model and how differences in representation may influence simulation results.

### Adhesion

Cell-cell adhesion is a fundamental property of tissue self-organization. If embryonic cells of two or more histological types are placed into contact with each other, they can undergo spontaneous reproducible patterns of rearrangement and sorting. This process can, for example, lead to engulfment of one cell type by another. Explanations for this phenomenon include the differential adhesion hypothesis, which states that cells tend to prefer contact with some cell types more than others due to type-specific differential intercellular adhesion [38]; and the differential interfacial tension hypothesis, which states that cells of different types instead exert different degrees of interfacial tension when in contact with other cell types or any surrounding medium [39]. Computational modelling has played a key role in comparing these hypotheses [40].

As our first case study, we simulate cell sorting due to differential adhesion in a monolayer of cells in the absence of cell proliferation or respecification. We consider a mixed population of two cell types, A and B, which we assume to exhibit differential adhesion. This is implemented in the CA, CP and VM models by having different values of the parameter  $\gamma$  for different cell types. Specifically, we choose  $\gamma(A, A) = \gamma(B, B) < \gamma(A, B)$  and  $\gamma(A, \text{void}) < \gamma(B, \text{void})$  to drive type-A cells to engulf type-B cells. In the cell-centre (OS and VT) models, we instead assume that for any pair of neighbouring cells located a distance farther apart than the rest length, the spring constant,  $\mu$ , is reduced by a factor  $\mu_{het} = 0.1$  if the cells are of different types. Additionally, in the OS model we use a larger interaction radius,  $r_{\max} = 2.5$ , to encourage cell sorting.

In addition to the update rules and equations of motion outlined in the previous section, we consider each cell to be subject to random motion. This random motion is intrinsic to the CA and CP models and is adjusted by changing the parameter  $T$  in Eqs (1) and (3). For the OS, VT and VM models we introduce an additional random perturbation force acting on each

cell or vertex,

$$\mathbf{F}^{\text{rand}} = \sqrt{\frac{2\xi}{\Delta t}} \boldsymbol{\eta}, \quad (12)$$

where  $\boldsymbol{\eta}$  is a vector of samples from a standard multivariate normal distribution and  $\xi$  is a parameter that represents the magnitude of the perturbation [35]. This size is scaled by the time step to ensure that when the equations of motion are solved numerically, the amplitude of the random perturbation force is independent of the size of time step. We simulate each model ten times, starting from an initial rectangular domain of width  $L_x$  and height  $L_y$ , comprising 50% type-A cells and 50% type-B cells. For all models, the edge of the domain is a free boundary, with no modification being made in the force (or update rule) on each boundary cell or vertex.

The time step of the CA and CP models dictates how many MCS occur per hour and, along with the temperature,  $T$ , can influence the dynamics of the simulation [37]. Here we perform an *ad hoc* calibration of  $T$  and  $\Delta t$  so that the temporal dynamics of the CA and CP models match those of the other models as far as possible [37]. A full list of parameter values is provided in Tables 1 and 2.

**Table 1. Table of parameters used in the models across case studies.**

Parameter	Description	Model(s)	Value	Reference
$\Delta t$	Time step	CA, CP	0.01 h	[37]*
		OS, VT, VM	0.005 h	[35] [30]
$A^{(0)}$	Cell target area	CA	1 LS (1.0 CD <sup>2</sup> )	—
		OS	$\pi/4$ CD <sup>2</sup>	—
		CP	16 LS (1.0 CD <sup>2</sup> )	—
		VT	$\sqrt{3}/2$ CD <sup>2</sup>	—
		VM	1 CD <sup>2</sup>	[35]
$C^{(0)}$	Cell target perimeter	CP	16 LS (4 CD)	[37]
		VM	$2\sqrt{\pi}$ CD	[35]
$\alpha$	Volume deformation coefficient	CP	0.1	[37]
		VM	50.0	[35]
$\beta$	Surface deformation coefficient	CP	0.01	[37]
		VM	1.0	[35]
$\gamma(\text{cell}, \text{cell})$	Cell-cell adhesion coefficient	CA, CP	0.1	[37]*
		VM	1	[35]
$\gamma(\text{cell}, \text{void})$	Cell-boundary adhesion coefficient	CA, CP	0.2	[37]*
		VM	10	[35]
$k_C$	Decay of attraction force	OS	5	[29]
$T$	Temperature	CA	0.0	—
		CP	0.1	[37]
$\eta$	Drag coefficient	OS, VT	1.0	[30]
		VM	1	[35]
$\mu$	Spring constant	OS, VT	50.0	[8], [41]
$s$	Mature cell spring rest length	OS, VT	1.0 CD	[30]
$K_{\text{swap}}$	rate of cell switching	CA	1	—
$r_{\text{max}}$	Force cut-off length	OS	1.5	—
$l_r$	Cell rearrangement threshold	VM	0.1 CD	[35]

Asterisks (\*) denote parameters whose values are taken for the CP model from the given reference, with the same value being assumed for the CA model.

doi:10.1371/journal.pcbi.1005387.t001

**Table 2. Table of parameters specific to the differential adhesion simulations.**

Parameter	Description	Model(s)	Value	Reference
$L_x$	Initial width of tissue	All	20 CD	—
$L_y$	Initial height of tissue	All	20 CD	—
$t_{cycle}$	Mean cell cycle duration	All	16 h	—
$t_{end}$	Simulation duration	All	100 h	—
$\gamma(A, B)$	Heterotypic cell-cell adhesion coefficient	CA	0.2	*
		CP	0.5	*
		VM	2	*
$\gamma(B, \text{void})$	Type B cell-boundary adhesion coefficient	CA	0.4	*
		CP	1.0	*
		VM	20	*
$\mu_{het}$	Heterotypic spring constant	OS, VT	0.1	[42]
$r_{\max}$	Force cut-off length	OS	2.5	*
$T$	Base 'temperature'	CA	0.1	*
		CP	0.2	[37]*
$\xi$	Base level of perturbation	OS	0.05	*
		VT	0.1	*
		VM	0.1	*
$k_{\text{pert}}$	Perturbation multiplier	All	$[10^{-2}, 10^2]$	—

Asterisks (\*) denote parameters whose values in the CA and CP models are chosen to ensure that engulfment occurs over a similar timescale to that observed in the OS, VT and VM models.

doi:10.1371/journal.pcbi.1005387.t002

The results of a single simulation of each model are shown in Fig 2. In each case, the tissue evolves to a steady state where cells of each type are more clustered than the initial configuration. In the CA, CP and VM models, type-A cells are eventually completely engulfed; note that for other parameter values, each model can exhibit dissociation or checkerboard patterning [4], [40]. In the other models, the tissue evolves to a local steady state (a dynamic equilibrium at a local minimum in the global energy landscape) that does not correspond to complete engulfment.

A quantitative comparison of cell sorting dynamics is shown in Fig 3. In particular we show how cell sorting is affected by the level of random motion applied to cells by multiplying the temperature  $T$  (for CA and CP simulations) or perturbation force magnitude  $\xi$  (for OS, VT and VM simulations) by the multiplier  $k_{\text{pert}}$  which we vary between  $10^{-2}$  and  $10^2$ . This is demonstrated by computing the fractional length, defined as the total length of edges between cells of different types for each simulation. These are then normalised by the length at  $t = 0$  for comparison. The dashed black line represents the fractional length for optimal engulfment (a circular region of 200 type A cells surrounded by type B cells). We find that the CA and CP models undergo repeated annealing due to their stochastic updating, and eventually end up at the global minimum (corresponding to complete engulfment). However, large amounts of noise can cause disassociation of cells in the CP model.

As Fig 3 (left) shows, for the off-lattice models the total energy of the system evolves to a local minimum in the absence of random cell movement. However, we can recover more complete engulfment through the addition of random cell movement. A relatively large amount of noise is required to alter cell neighbours in the Delaunay triangulation, illustrated by the flat lines in Fig 3 (Left, VT). However, if there is too much noise then cells can become dissociated and move amongst the ghost nodes; in this case, if a cell reaches the edge of the ghost node region, its

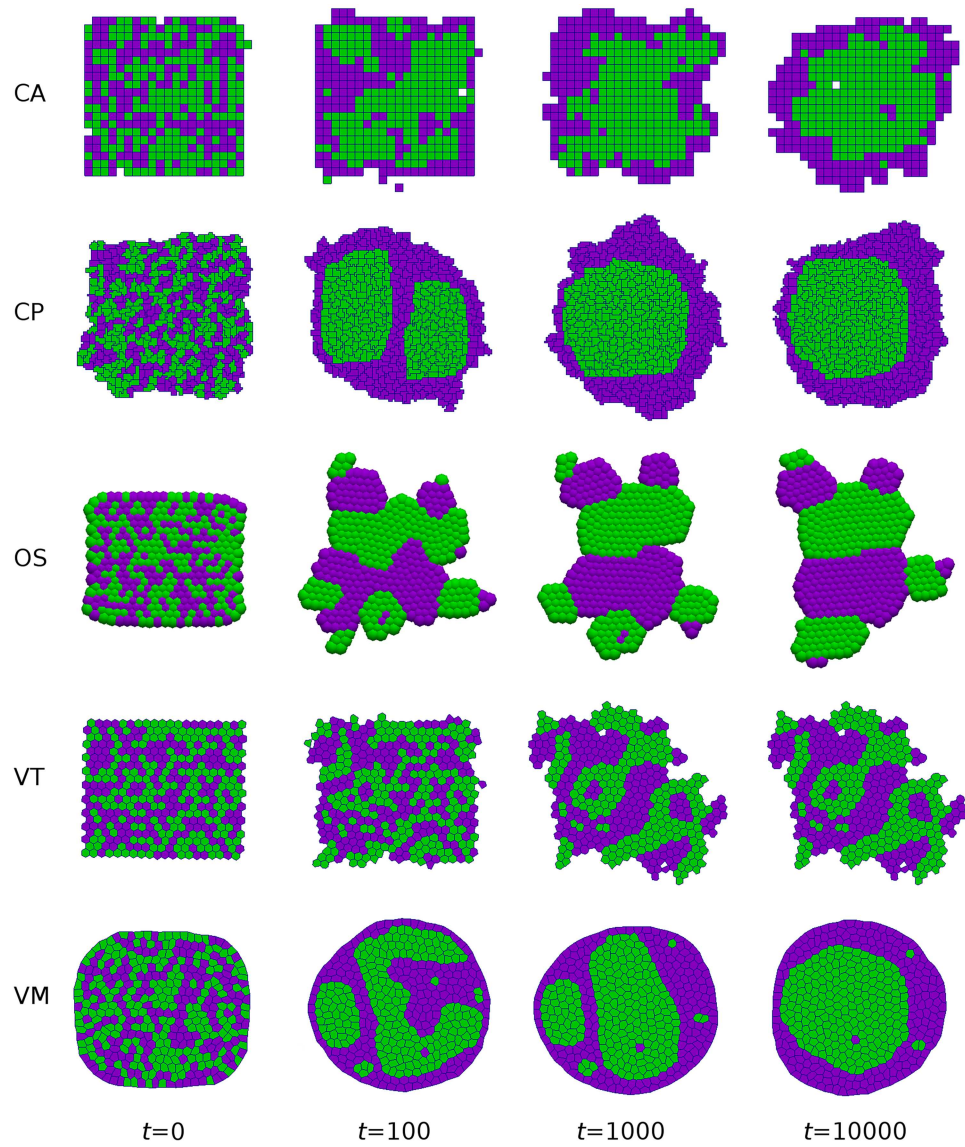


**Fig 2. Simulations of cell sorting due to differential adhesion.** Snapshots are shown at selected times for each model. Cells of type A and B are shown in purple and green, respectively. Engulfment of type-B cells occurs most readily in the CA, CP and VM models. Parameter values are given in Tables 1 and 2, with  $k_{\text{pert}} = 1$ . A video of these simulations is given in [S1 Movie](#).

doi:10.1371/journal.pcbi.1005387.g002

Voronoi area becomes ill-defined and we can no longer define the fractional length and therefore halt these simulations. A similar sensitivity is exhibited by the VM; in this case, if the amount of noise is too high, cell shapes can become inverted due to vertices randomly intersecting edges, again we halt these simulations if this occurs. From the fractional length plots it is clear that for certain simulations there is an increased level of fluctuation in fractional length. In [Fig 3](#) (right) we present how the level of fluctuation in fractional length varies as we increase the perturbations applied to the models. We calculate the magnitude of the fluctuations as the mean squared error between the original curves and smoothed versions of the same curves, using a 10 hour smoothing range. For all models the magnitude of the fluctuations increases as  $k_{\text{pert}}$  is

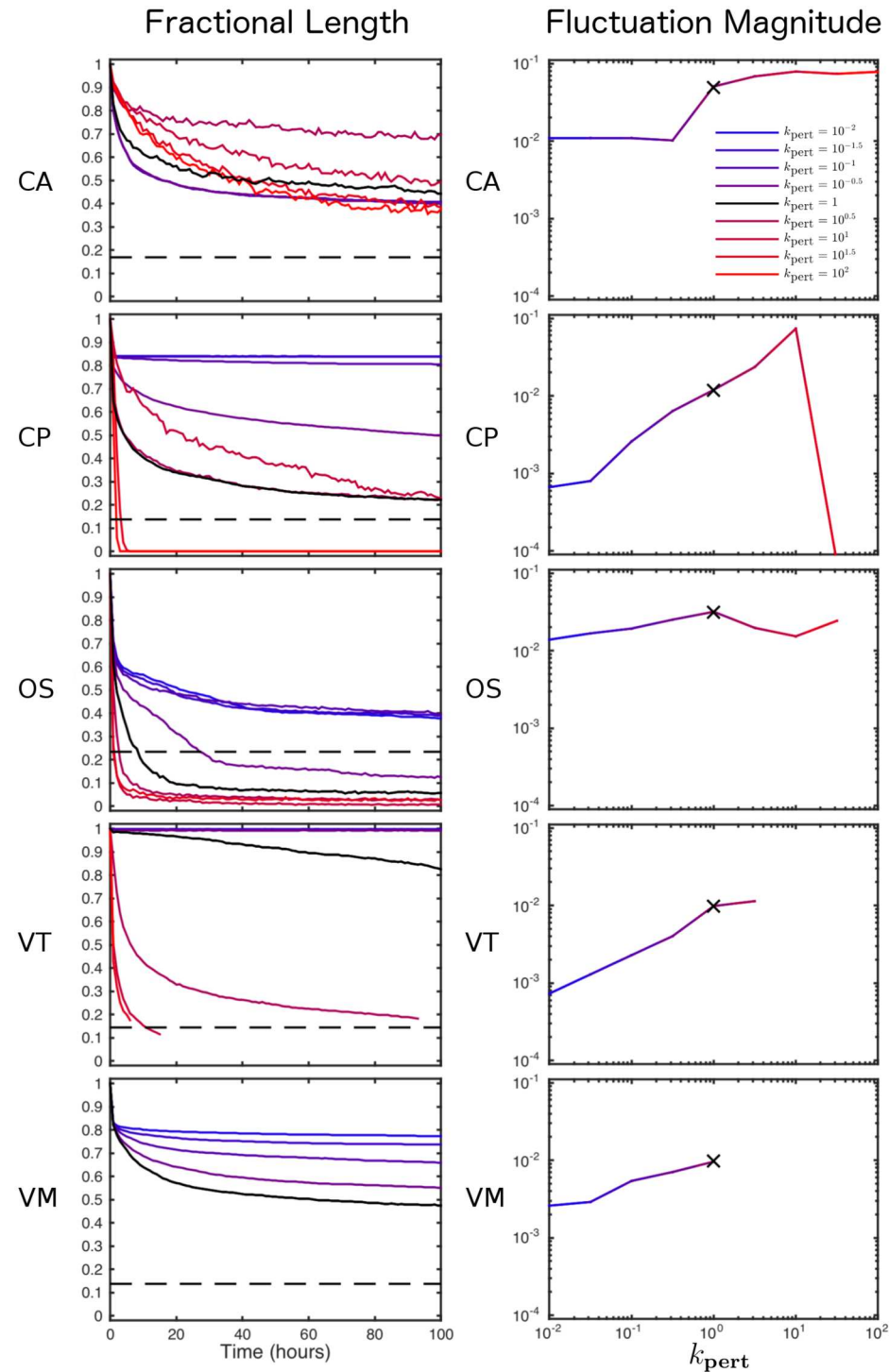


**Fig 3. Comparison of cell sorting dynamics across differential adhesion simulations.** Left, as a measure of sorting, the fractional length is computed as a function of time for each model. Results are shown for varying multiples of the baseline level of noise,  $T$  or  $\xi$  (whose value is defined for each model in Table 2), by multiplying by  $k_{\text{pert}}$ . Each line is the mean value of 10 simulations. Right, the magnitude in the fluctuation of the fractional length curves (calculated as the mean squared error between the original curves and smoothed versions of the same curves, using a 10 hour smoothing range). The simulations from Fig 2 (with  $k_{\text{pert}} = 1$ ) are denoted, on the left and right, by black lines and black crosses, respectively. Parameter values are given in Tables 1 and 2.

doi:10.1371/journal.pcbi.1005387.g003

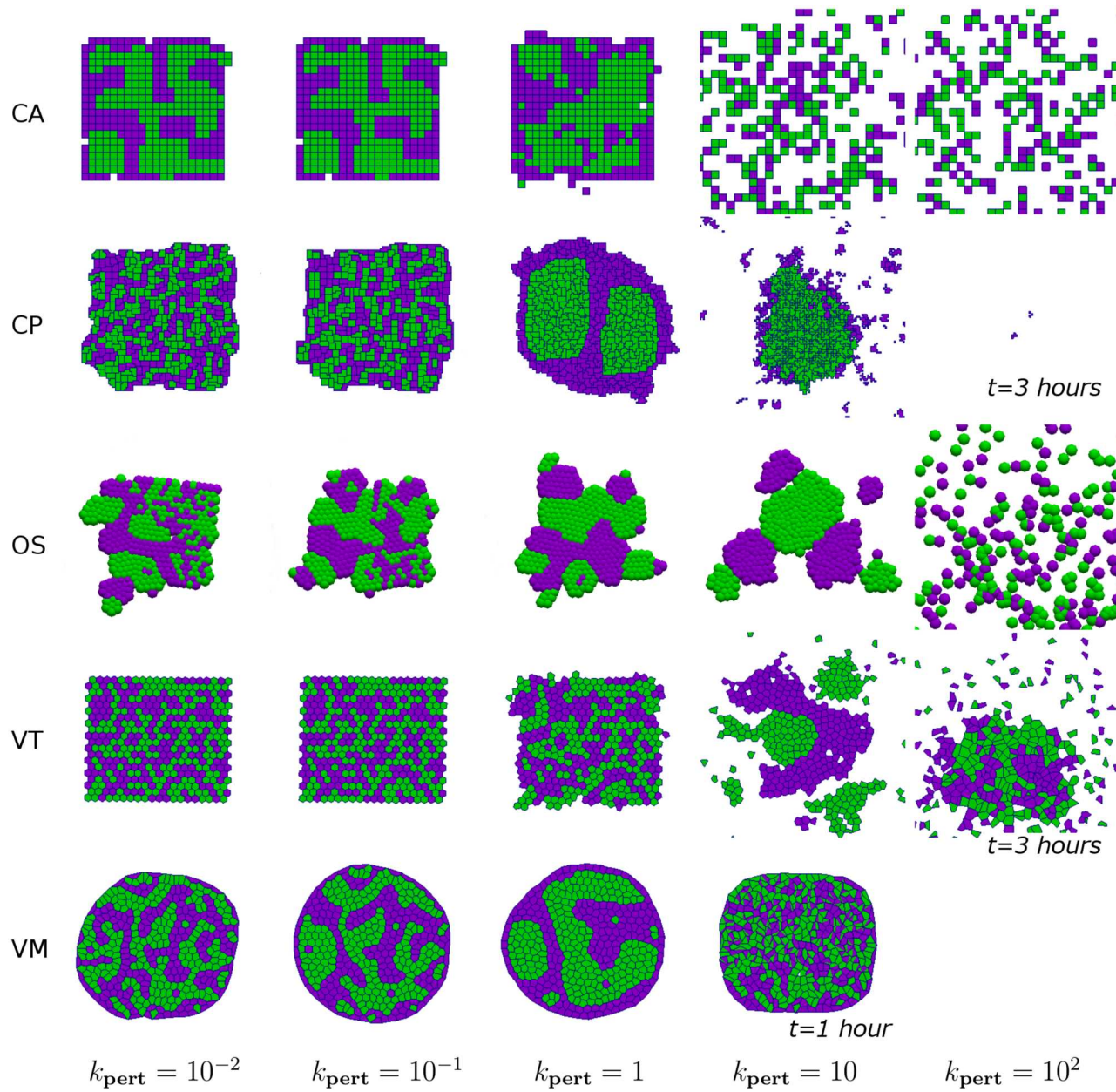


**Fig 4. Effect of perturbations on cell sorting.** Snapshots at  $t = 100$  (unless otherwise indicated) for the simulations presented in Fig 2 for varying  $k_{\text{pert}} = 10^{-2}, 10^{-1}, 1, 10, 10^2$ . Parameter values are given in Tables 1 and 2. For CP simulations with  $k_{\text{pert}} = 10^2$  a snapshot is given at  $t = 3$  as by this time in the simulation cells are already dissociated and have left the viewing window. For VT simulations with  $k_{\text{pert}} = 10^2$  a snapshot is given at  $t = 3$  as by this time in the simulation a cell has left the tissue domain and caused an infinite Voronoi region and the simulation is halted. For VM simulations with  $k_{\text{pert}} = 10^1$  a snapshot is given at  $t = 1$  as by this time in the simulation the perturbations cause cells to become inverted and the simulation is halted. There is no plot for VM simulations with  $k_{\text{pert}} = 10^2$  as for this level of perturbation cells become inverted at the first time step so the simulations are not run. Note the central column corresponds to the  $t = 100$  snapshots in Fig 2.

doi:10.1371/journal.pcbi.1005387.g004

increased. The exception to this is that the fluctuations for CP simulations for large  $k_{\text{pert}}$  are effectively zero, this is because cells have become dissociated and the fractional length is zero.

In order to illustrate the effect of perturbations on the patterning of the tissue, in Fig 4 we present snapshots of the tissue at  $t = 100$  (where possible) for increasing levels of perturbation ( $k_{\text{pert}}$ ). We see that for each model as we increase the perturbation we move from an unsorted

state to the sorted states presented in Fig 2 but as we increase the perturbations further cells become dissociated, and for VT and VM models assumptions of connectivity and concavity of cells can become void (shown by incomplete lines in Fig 3 and missing snapshots in Fig 4).

To summarise, we find that the degree of cell sorting observed in our simulations depends on how much random cell movement can be accommodated within each model. We note that there is no reason *a priori* to suppose that the configuration corresponding to the global minimum is biologically realistic; this depends on how the typical time scale which complete sorting occurs compares to other embryogenic processes. Comparing the different models, we note that the OS and VT models considered in Fig 2 will always differ from the CA, CP and VM models, in that given sufficient time they will fully separate rather than undergo complete engulfment.

### Proliferation, death and differentiation

Embryonic development and adult tissue self-renewal both rely on careful control of cell proliferation, differentiation and apoptosis to ensure correct cell numbers. The intestinal epithelium offers a particularly well-studied example of such tightly orchestrated cell dynamics. It is folded to form invaginations called crypts and (in the small intestine) protrusions called villi. The disruption of cell proliferation and migration in intestinal crypts is the cause of colorectal cancers. Experimental evidence indicates a complex pattern of cell proliferation within the crypt, in which cells located at the base of the crypt cycle significantly more slowly than those further up. One possible explanation for this is contact inhibition, in which stress due to overcrowding causes a cell to proliferate more slowly, enter quiescence or even undergo apoptosis [43]. The biological mechanism through which shear stress affects the expression of key components in the Wnt signalling pathway, which in turn plays an important role in cell proliferation and adhesion in this tissue, has been elucidated through a number of studies [44], [45].

A variety of cell-based models have been developed to study aspects of intestinal crypt dynamics [46], including defining the role of the Wnt signalling pathway [47]. The process and consequences of contact inhibition have also been described using cell-based modelling approaches in a more general setting [48], [49], [50]. A recent study used a cell-centre modelling approach to investigate how combined changes in Wnt signalling response and contact inhibition may induce altered proliferation in radiation-treated intestinal crypts [42].

As our second case study, we simulate the spatiotemporal dynamics of clones of cells within a single intestinal crypt. This example demonstrates how multicellular models and simulations (in particular Chaste) can include the coupling of cell-level processes to simple subcellular processes and deals with cell proliferation, death and differentiation.

Our underlying model of a colonic crypt has been described in detail previously [31], [51], [52]. We restrict cells to lie on a fixed cylindrical crypt surface, defined by the two-dimensional domain  $[0, L_x] \times [0, L_y]$ , where  $L_x$  and  $L_y$  denote the crypt's circumference and height, respectively. Periodicity is imposed at the left- and right-hand boundaries  $x \in \{0, L_x\}$ . We impose a no-flux boundary condition at the crypt base ( $y = 0$ ) and remove any cell that reaches the crypt orifice ( $y = L_y$ ). In each simulation, we start with a regular tessellation of cells occupying this domain; the crypt is then evolved for a duration  $t_{start}$  to a dynamic equilibrium, before cell clones are recorded and the crypt evolved for a further duration  $t_{end}$ .

For each cell-based model considered, we implement cell proliferation and differentiation as follows. Any cell located above a threshold height  $y_{prolif}$  from the crypt base is considered to be terminally differentiated, and can no longer divide. Any cell located below  $y_{prolif}$  can proliferate. On division a random cell cycle duration is drawn independently for each daughter cell. Specifically, we draw the duration of each cell's G1 phase,  $t_{G1}$ , from a truncated normal

**Table 3. Table of parameters specific to the colonic crypt simulations.**

Parameter	Description	Model(s)	Value	Reference
$t_{\text{start}}$	Pre-simulation duration	All	100 h	—
$t_{\text{end}}$	Simulation duration	All	1000 h	—
$r_{CI}$	Quiescent volume fraction	All	0–1	—
$L_x$	Width of crypt	All	15 CD	Scaled from [41]
$L_y$	Height of crypt	All	12 CD	Scaled from [41]
$h$	Height at which cells are sloughed	All	12 CD	Scaled from [41]
$\mu_{G1}$	G1 phase duration mean	All	2 h	—
$\sigma_{G1}^2$	Cell cycle variance	All	1 h	—
$t_{G1,\text{min}}$	Minimum G1 Phase duration	All	0.01 h	—
$t_S$	S Phase duration	All	5 h	—
$t_{G2}$	G2 Phase duration	All	4 h	—
$t_M$	M Phase duration	All	1 h	—
$y_{\text{prolif}}$	Proliferation height threshold	All	6 CD	Scaled from [41]

doi:10.1371/journal.pcbi.1005387.t003

distribution with mean  $\mu_{G1} = 2$ , variance  $\sigma_{G1}^2 = 1$  and lower bound  $t_{G1,\text{min}} = 0.01$ , and we set the remainder of the cell cycle as  $t_S = 5$ ,  $t_{G2} = 4$  and  $t_M = 1$ , for the durations of the S phase, G2 phase, and M phase, respectively.

In addition the duration of G1 phase depends on the local stress, interpreted as the deviation from a cell's preferred area. A cell pauses in the G1 phase of the cell cycle if

$$A_i < r_{CI} A_i^{(0)}, \quad (13)$$

where  $r_{CI}$  is the quiescent area fraction and  $A_i$ ,  $A_i^{(0)}$  is as earlier defined for each model [53]. This description allows for quiescence imposed by transient periods of high compression, followed by relaxation. If a cell is compressed during the G2 or S phases then it will still divide, and thus cells whose areas are smaller than the given threshold may still divide.

The dimensions of the crypt domain are chosen in line with [41] but are scaled to decrease simulation time. A full list of parameter values is provided in Tables 1 and 3.

The results of a single simulation of each model are shown in Fig 5. In each case, the number of clones decreases over time as the crypt drifts to monoclonality. A more quantitative comparison of clonal population dynamics is shown in the left column of Fig 6. For each simulation we compute the number of clones remaining in the crypt as a function of time. All models exhibit the same qualitative behaviour, with a sharp initial drop as all clones corresponding to cells outside the niche are rapidly lost, followed by a more gradual decay in the number of clones at the crypt base due to neutral drift. However, we note that the number of clones reduces more slowly in the VM than other models, since the implementation of the 'no flux' boundary condition at the crypt base causes cells to remain there for longer in this model. This highlights the effect that the precise implementation of boundary conditions can have in such models. Finally, we note that for models where contact inhibition can be imposed, we see a slight effect of the degree of contact inhibition on the clonal population dynamics. In most of the models contact inhibition slows the process of monoclonal conversion, due to there being more compression at the crypt base. In contrast, in the VM the number of clones present in the crypt decreases more quickly when  $r_{CI}$  is larger. This effect is due to there being higher rates of division, resulting in cells more frequently being 'knocked' from the crypt base; in the other models this effect is counteracted by compression from above.

A quantitative comparison of cell velocity profiles up the crypt is shown in the right column of [Fig 6](#). Additionally we present the average number of cells in the crypt for all simulations in [Fig 7](#). This extends the comparison previously made of cell-centre and vertex models of crypt dynamics in [51]. For each simulation we compute the vertical component of cell velocity at different heights up the crypt, averaging over the  $x$  direction. We find that all models are similar when considering a ‘position-based’ cell-cycle model (in which cell proliferation occurs below a threshold height up the crypt, corresponding to a threshold Wnt stimulus). However we see more pronounced differences when incorporating more restrictive contact inhibition into the cell-cycle model, in particular we see that the VT model is affected much more than the other models and the CA model is unaffected (as all cells have the same constant size). This is because, with the parameters being used, cells in the VT model are more compressed than in the other models, as seen by the increased number of cells in the simulation (shown in [Fig 7](#)). Due to this increased compression a greater number of cells experience contact inhibition. In fact the OS cells are also as compressed (as seen by a similar number of cells) but due to the different calculation of cell area fewer cells experience contact inhibition and therefore the velocity is influenced less than in the VT model.

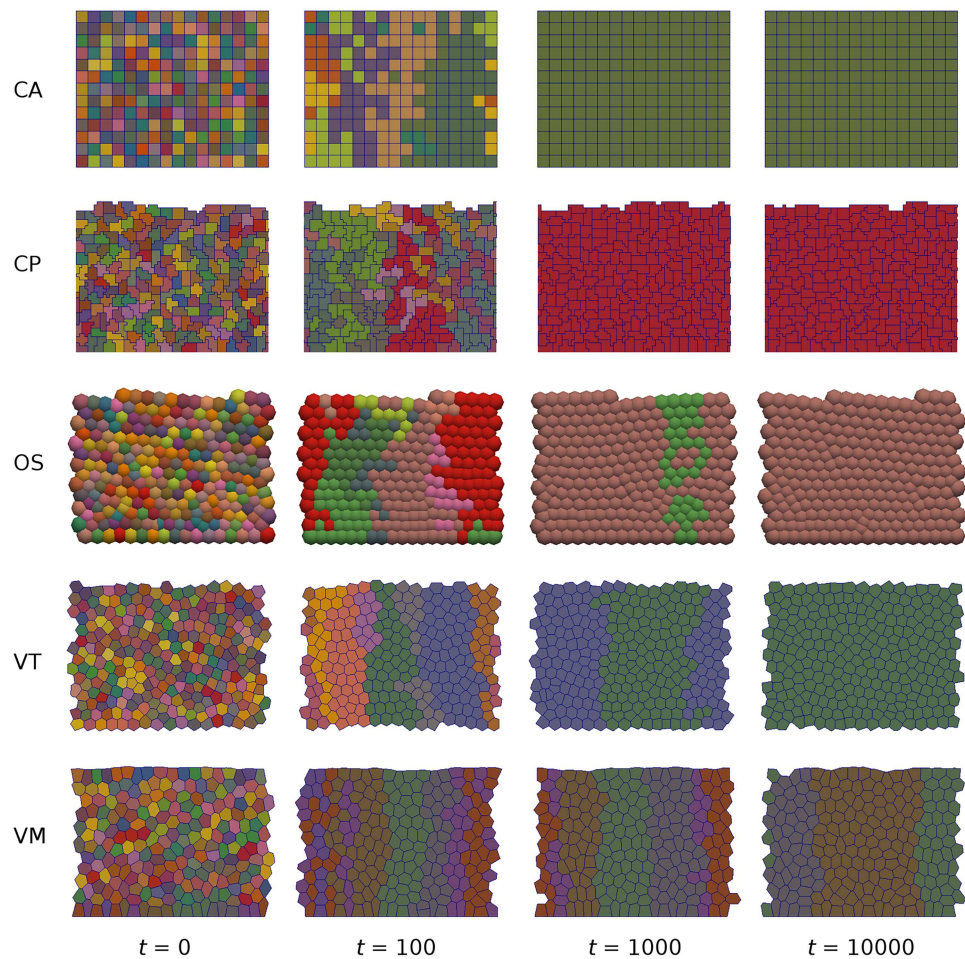


**Fig 5. Simulations of monoclonal conversion in the colonic crypt.** Snapshots are shown at selected times for each model. In each simulation at time  $t=0$ , every cell is regarded as a clonal population and given a different colour, which is inherited by its progeny. These populations evolve in time due to cell proliferation and sloughing from the crypt orifice, resulting in a single clone eventually taking over the entire crypt. Parameter values are given in Tables 1 and 3, with  $r_{CI} = 0.8$ . A video of these simulations is given in [S2 Movie](#).

doi:10.1371/journal.pcbi.1005387.g005

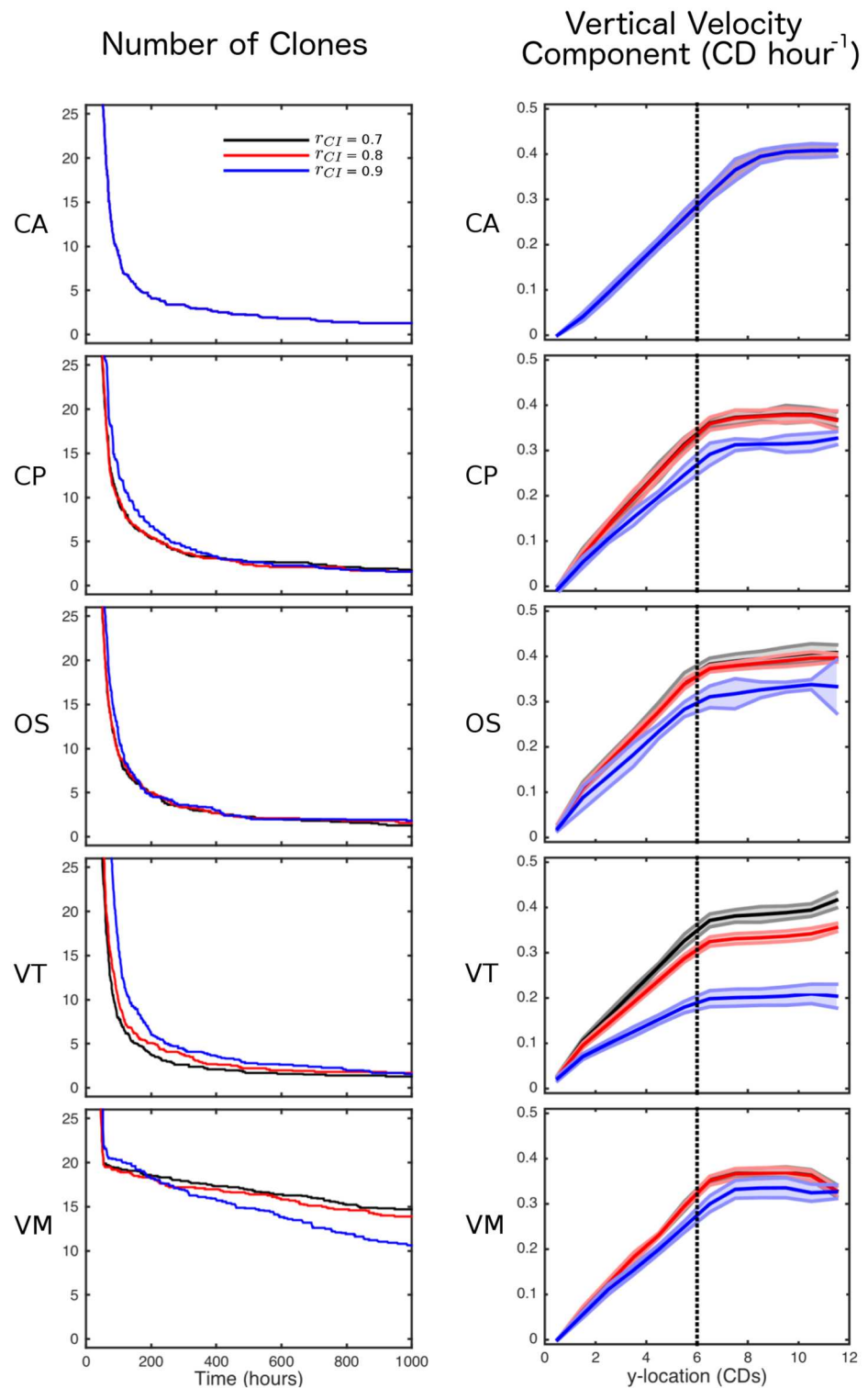


**Fig 6. Comparison of clonal population dynamics and cell velocity across crypt simulations for varying levels of contact inhibition.** Left: the number of clones remaining in the crypt is computed as a function of time for each model: CA; CP; OS; VT; and VM. Right: the vertical component of cell velocity is computed for each model. For each model, the mean and standard error (not shown on clonal plots for clarity) from 10 simulations are shown for three levels of contact inhibition, quantified by the parameter  $r_{CI}$ . The vertical dotted line corresponds to the height of the proliferative compartment,  $y_{prolif}$ . Parameter values are given in Tables 1 and 3.

doi:10.1371/journal.pcbi.1005387.g006

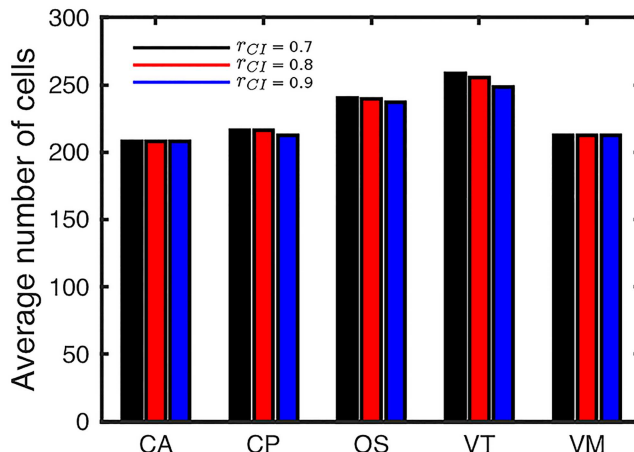


**Fig 7. Number of cells in the crypt for varying contact inhibition.** For each model, the mean number of cells from 10 simulations are shown for three levels of contact inhibition, quantified by the parameter  $r_{CI}$ . Parameter values are given in Tables 1 and 3.

doi:10.1371/journal.pcbi.1005387.g007

### Short-range signalling

In many developmental processes, distinct states of differentiation emerge from an initially uniform tissue. Lateral inhibition, a process whereby cells evolving towards a particular fate inhibit their immediate neighbours from doing so, has been proposed as a mechanism for generating such patterns. This process is known to be mediated by the highly conserved Notch signalling pathway, which involves ligand-receptor interactions between the transmembrane proteins Notch and Delta or their homologues [54].

Lateral inhibition through Notch signalling has been the subject of several mathematical modelling studies [55], [56], [57], [58], [59], [60]. Such models have largely focused on the conditions for fine-grained patterns to occur in a fixed cell population; little attention has been paid to its interplay with cell movement, intercalation and proliferation. To illustrate how cell-based modelling approaches may be utilised to investigate such questions, as our third case study we simulate Notch signalling in a growing monolayer. This example demonstrates how intercellular signalling may be incorporated within each cell-based model.

In this example, cells proliferate if located within a radius  $R_P$  from the origin, and are removed from the simulation if located more than a radius  $R_S > R_P$  from the origin. For each proliferative cell, we allocate a probability  $p_{div}$  of division per hour, once the cell is above a minimum age,  $t_{min}$ . This is implemented by independently drawing a uniform random number  $r \sim U[0, 1]$  for each cell at each time step and executing cell division if  $r < p_{div}\Delta t$ .

This description is coupled to a description of Notch signalling between neighbouring cells that is based on a simple ordinary differential equation model previously developed by Collier et al. [55]. This represents the temporal dynamics of the concentration of Notch ligand,  $N_i(t)$ , and Delta receptor,  $D_i(t)$ , in each cell  $i$  in the tissue. A feedback loop is assumed to occur, whereby activation of Notch inhibits the production of active Delta. Signalling between cells is reflected in the dependence of Notch activation on the average level of Delta among a cell's immediate neighbours. The precise set of equations for this signalling model takes the form

$$\frac{dN_i}{dt} = \frac{\bar{D}_i^{n_N}}{k_N + \bar{D}_i^{n_N}} - N_i, \quad (14)$$

$$\frac{dD_i}{dt} = r_{DN} \left( \frac{k_D}{k_D + N_i^{n_D}} - D_i \right), \quad (15)$$

where  $\bar{D}_i$  denotes the average value of  $\{D_j(t) : j \in \mathcal{N}_i(t)\}$ , and  $\mathcal{N}_i(t)$  is the set of neighbours of cell  $i$ . A full list of parameter values is provided in Tables 1 and 4. At the start of the simulation, values of each  $N_i$  and  $D_i$  are independently drawn from a  $U[0, 1]$  distribution. Upon division, the values of  $N_i$  and  $D_i$  are inherited by each daughter cell.

Eqs (14) and (15) are coupled to the cell-based models using the following algorithm. At each time step, having updated the cell-based model, we calculate  $\bar{D}$  based on the current connectivity and, assuming  $\bar{D}$  remains constant on the short interval  $\Delta t$ , we solve the Notch signalling model numerically over the interval  $[n\Delta t, (n + 1)\Delta t]$  using a Runge-Kutta method. In terms of software implementation, all Delta-Notch simulations share a common function that contains just a few lines for initialising the subcellular level of Delta-Notch.

Simulation snapshots for each model are shown in Fig 8. In each case, we see that lateral inhibition successfully leads to patterning of cells in ‘high Delta’ steady state surrounded by cells in a ‘low Delta’ steady state in the outer ring of non-proliferating cells. This patterning is disrupted in the inner proliferating region, as cells frequently change neighbours and hence are unable to synchronise their Delta-Notch dynamics. The degree of this disruption increases with cell division rate and is most apparent in the VM simulation. A lattice-induced anisotropy is clearly visible in the CA simulation, where cell shoving causes significantly more cell rearrangements and, as a result, less patterning along diagonals. This phenomenon also occurs, to a lesser extent, in the CP simulation.

A quantitative comparison of the patterning dynamics across models is shown in Fig 9 (Left). As a measure of patterning we plot the ratio of cells in the heterogeneous steady state to those not in this state at the end of each simulation, computed as a radial distribution across the tissue. Note that the ‘kinks’ observed in the CA results (Fig 9(Left CA)) are due to the presence of discrete cells on a fixed lattice. We also present the level of cell compression (represented as the number of cells per unit target area, for each model, as proliferation is varied in Fig 9(Right)). We see that there is significantly less patterning in the proliferative region for all models and that as the rate of division is increased the difference is exaggerated. This is due to cells becoming more compressed in the central proliferative zone (Fig 9(Right)) and causing cells to expand outwards faster. For higher proliferation rates this leads to exchanging neighbours more frequently, even in regions without proliferation. This is most apparent in the VT and VM simulations where there is a larger degree of compression in the proliferative zone. Note that several of the models show an increase in cell numbers (per unit target area) on the edge of the tissue. This is due to cells being removed once the center of the cell had passed the right of the outer-most bin which allows more cell centers in the outer-most bin without being compressed.

## Long-range signalling

Morphogens are secreted signalling molecules that provide positional information to cells in a developing tissue and act as a trigger for cell growth, proliferation or differentiation. The processes of morphogen gradient formation, maintenance and interpretation are well studied, most notably in the wing imaginal disc in the fruit fly *Drosophila* [61], a monolayered epithelial tissue. A key morphogen called Decapentaplegic (Dpp) forms a morphogen gradient along the anterior-posterior axis of this tissue. Dpp is known to determine the growth and final size of the wing imaginal disc, although the mechanism by which its gradient is established remains unclear.

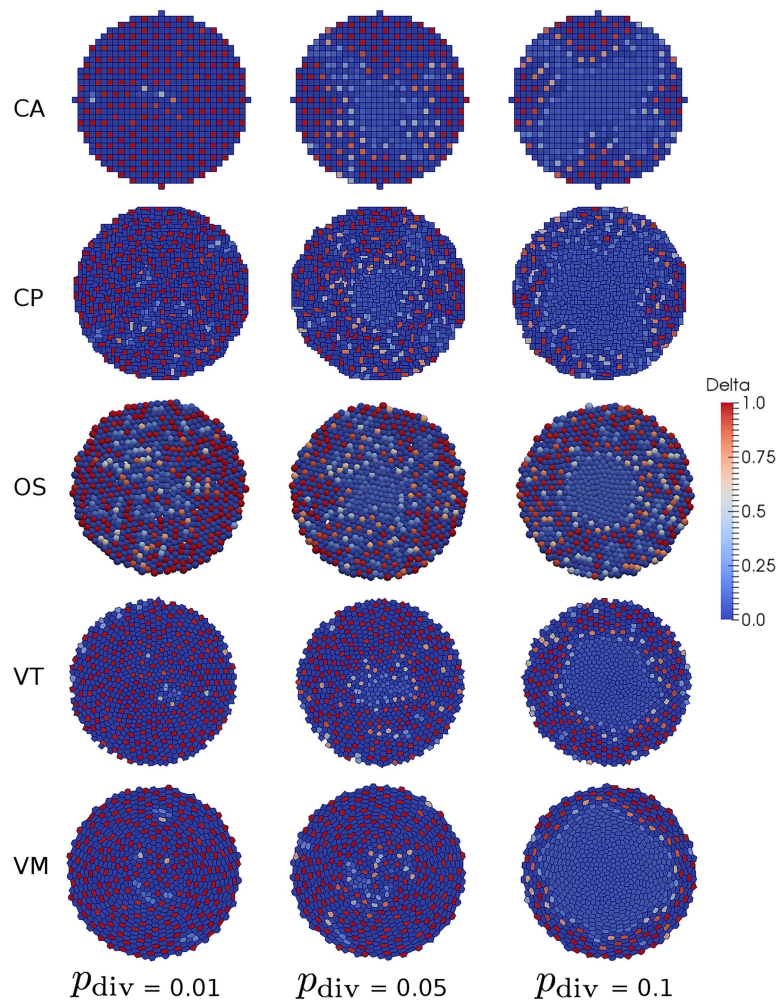


**Fig 8. Simulations of lateral inhibition in a proliferating tissue.** For each model, snapshots are shown for three levels of cell proliferation, quantified by the parameter  $p_{\text{div}}$ . Parameter values are given in Tables 1 and 4. A video of these simulations, for  $p_{\text{div}} = 0.1$ , is given in [S3 Movie](#).

doi:10.1371/journal.pcbi.1005387.g008

**Table 4. Table of parameters specific to the lateral inhibition simulations.**

Parameter	Description	Model(s)	Value	Reference
$t_{\text{end}}$	Simulation duration	All	1000 h	—
$t_{\text{steady}}$	Time simulations are in dynamic equilibrium	All	200 h	—
$p_{\text{div}}$	Cell division rate	All	$\{0.01, 0.05, 0.1\} \text{ cell}^{-1} \text{ h}^{-1}$	—
$t_{\text{min}}$	Minimum division age	All	1 h	—
$k_N$	Dependence of Notch on Delta	All	0.01	[55]
$k_D$	Dependence of Delta on Notch	All	0.01	[55]
$n_N$	Notch Hill coefficient	All	2	[55]
$n_D$	Delta Hill coefficient	All	2	[55]
$r_{DN}$	Relative rate of Delta activity	All	$1 \text{ h}^{-1}$	[55]
$R_P$	Radius of proliferative compartment	All	5 CD	—
$R_S$	Removal zone radius	All	15 CD	—
$r_{\text{max}}$	Force cut-off length	OS	1 CD	—

doi:10.1371/journal.pcbi.1005387.t004

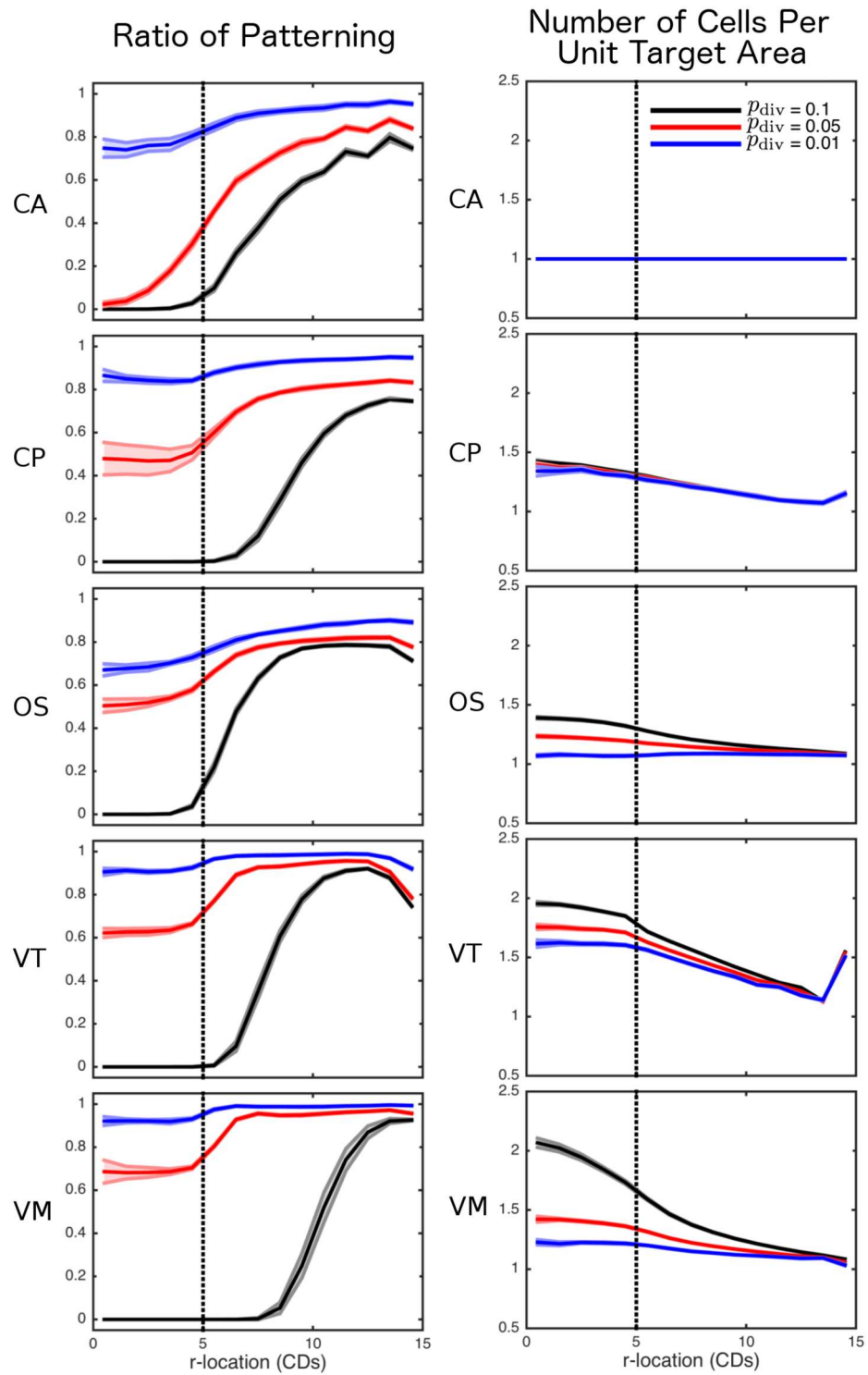


**Fig 9. Comparison of cell fate patterning, and cell compression across lateral inhibition simulations.** Left: as a measure of patterning, the ratio of cells in the heterogeneous steady state to those not in this state is computed, by averaging across times  $t = t_{\text{steady}}$  to  $t = t_{\text{end}}$ , as a radial distribution across the tissue (calculated using a bin size of 1 CD) for each model: CA; CP; OS; VT; and VM. Right: as a measure of compression, the number of cells per unit target area, for each model, is averaged as for the patterning ratios. For each model, the mean and standard error from 10 simulations are shown for three levels of cell proliferation, quantified by the parameter  $p_{\text{div}}$ . The vertical dotted line corresponds to the radius of the proliferative compartment,  $R_P$ . Parameter values are given in Tables 1 and 4.

doi:10.1371/journal.pcbi.1005387.g009

A number of cell-based models have been proposed for the cellular response to morphogen gradients and mechanical effects in developing tissues such as the wing imaginal disc [62], [63], [18]. As our final case study, we simulate the growth of an epithelial tissue in which cell proliferation is coupled to the level of a diffusible morphogen. This case study represents an abstraction of a wing imaginal disc and illustrates how continuum transport equations may be coupled to cell-based models.

Our description of morphogen-dependent cell proliferation is based on that proposed by [19] and is implemented as follows. The probability of a cell dividing exactly  $n$  time steps after its last division is given by  $p_{\text{div}}u_n\Delta t$ , where  $p_{\text{div}}$  is a fixed parameter and the weighting  $u_n$  satisfies the recurrence relation

$$u_{n+1} = u_n(1 + \Delta t g(1 + \lambda c_n)(1 - u_n)), \quad (16)$$

with  $u_0 = u_N/2$  where  $u_N$  denotes the parent cell's weighting value immediately prior to division. Here  $\lambda$  is a fixed parameter quantifying the effect of the morphogen on cell growth,  $c_n$  denotes the morphogen concentration at that cell at that time step, and  $g$  is a random variable independently drawn upon division from a truncated normal distribution with mean  $\mu_g$ , variance  $\sigma_g^2$  and minimum value  $g_{\min}$ .

When initialising the simulation, a value of  $g$  is drawn independently for each cell from a truncated normal distribution (as on division), and a value of  $u_0$  is drawn independently from a  $U[0.5, 1]$  distribution.

Each cell-based model is coupled to a continuum model of morphogen transport based on that proposed by [19]. We assume that the morphogen is secreted in a central 'stripe' of tissue and diffuses throughout the whole tissue, being transported by the cells, while being degraded. In this description, the morphogen concentration  $c(\mathbf{x}, t)$  is defined continuously for times  $t \geq 0$  in the spatial domain  $\mathbf{x} \in \Omega$ , defined by the boundary of the cell population (see below). This concentration evolves according to the reaction-advection-diffusion equation

$$\frac{\partial c}{\partial t} + \mathbf{w} \cdot (\nabla c) - \nabla \cdot (D \nabla c) = f(\mathbf{x}) - k_c c, \quad (17)$$

with zero-flux boundary conditions at the edge of the domain. In line with most work, we do not account for the exclusion of diffusing chemicals from the space occupied by cells. The vector field  $\mathbf{w}$  denotes the velocity of the cells moving in the tissue (and is found in the weak formulation in [19]). Its inclusion in Eq (17) denotes the advection of Dpp with the cells. The parameters  $D$  and  $k_c$  denote the morphogen diffusion coefficient and degradation coefficient, respectively. Finally, the function  $f$  specifies the rate of production of morphogen in the central stripe of tissue, and is given by

$$f(x, y) = \begin{cases} f_{\text{prod}} & \text{for } x \in (-L_{\text{prod}}, L_{\text{prod}}), \\ 0 & \text{otherwise.} \end{cases} \quad (18)$$

To solve Eq (17) numerically, we first discretise the spatial domain defined by the cells to make a computational mesh. For the VT model we use the triangulation defined by the dual of the Voronoi tessellation; for the vertex model we use the triangulation defined by dividing each polygonal cell into a collection of triangles (made up from the set of vertices and the centre of the polygon) as in [19]; and for the CA, CP and OS models we create a triangulation by calculating the constrained Delaunay triangulation of the centres of the cells. This tessellation changes over time as the tissue grows.

**Table 5. Table of parameters specific to the morphogen-dependent proliferation simulations.**

Parameter	Description	Model(s)	Value	Reference
$\Delta t$	Time step	All	0.005 h	—
$t_{\text{end}}$	Simulation duration	All	100 h	—
$L_r$	Initial radius of tissue	All	5 CD	[19]
$D$	Dpp diffusion coefficient	All	$10^{-4} \text{ CD}^2 \text{h}^{-1}$	[19]
$k_c$	Dpp degradation rate	All	$0.01 \text{ h}^{-1}$	[19]
$f$	Maximal Dpp production rate	All	$0.01 \text{ h}^{-1}$	[19]
$W_{\text{Dpp}}$	Width of Dpp production zone	All	4 CD	[19]
$p_{\text{div}}$	Average baseline cell division rate	All	$0.1 \text{ h}^{-1}$	[19]
$\lambda$	Morphogen effect on cell growth	All	0.01	[19]
$f_{\text{prod}}$	Level of production of Dpp in sripe	All	0.01	[19]
$L_{\text{prod}}$	Half the width of stripe of Dpp production	All	2 CD	[19]
$\mu_g$	Cellular growth rate mean	All	0.05	—
$\sigma_g^2$	Cellular growth rate variance	All	0.0001	—
$g_{\text{min}}$	Minimum cellular growth rate	All	0.01	—

doi:10.1371/journal.pcbi.1005387.t005

We solve [Eq \(17\)](#) using a method of lines approach along the characteristic curves

$$\frac{dc}{dt} = \frac{\partial c}{\partial t} + \mathbf{w} \cdot (\nabla c), \quad (19)$$

and a continuous Galerkin finite element approximation to the spatial derivatives.

We approximate the solution of [Eq \(17\)](#) using a Forward Euler discretization for time and a linear finite element approximation in space. As we generate the computational mesh from the cells, the mesh moves with velocity  $\mathbf{w}$ . We can therefore account for the advective term of [Eq \(17\)](#) by moving the solution with the moving cells. Finally in each model when a cell divides it creates a new node in the mesh and the solution at the new node is defined to be the same as the node attached to the parent cell. A full list of parameter values is provided in Tables 1 and 5.

Simulation snapshots for each model are shown in [Fig 10](#). As expected, over time the morphogen biases the shape of the tissue, which exhibits greater growth in the  $y$  direction. This is confirmed in [Fig 11](#) (right), which shows a quantitative comparison of tissue shape dynamics across models. A quantitative comparison of the spatio-temporal morphogen dynamics across models is shown in [Fig 11](#) (left). In each case, the morphogen distribution is plotted at different times as an average over the  $x$  direction and over 20 simulations. While the mean behaviour is conserved across models, the CA exhibits significantly greater variation about this mean. This is due to the discrete nature of cell movement, and hence morphogen advection, in these models. We would expect this greater variation to be less pronounced if a simpler approach often taken when simulating CA models, that of neglecting advection due to cell movement, were taken. Looking at the snapshots in [Fig 10](#) we see that despite being an off-lattice model the VT model exhibits some regularity in shape through growth, witnessed by straighter than expected edge segments (shown in detail in [Fig 12](#)). This is due to the method for calculating connectivity in the VT model and can introduce artefacts when considering freely growing domains as seen here.

## Discussion

The field of mathematical modelling in biology has matured beyond recognition over the past decade. One indication of this is the move towards quantitative comparison with data taking

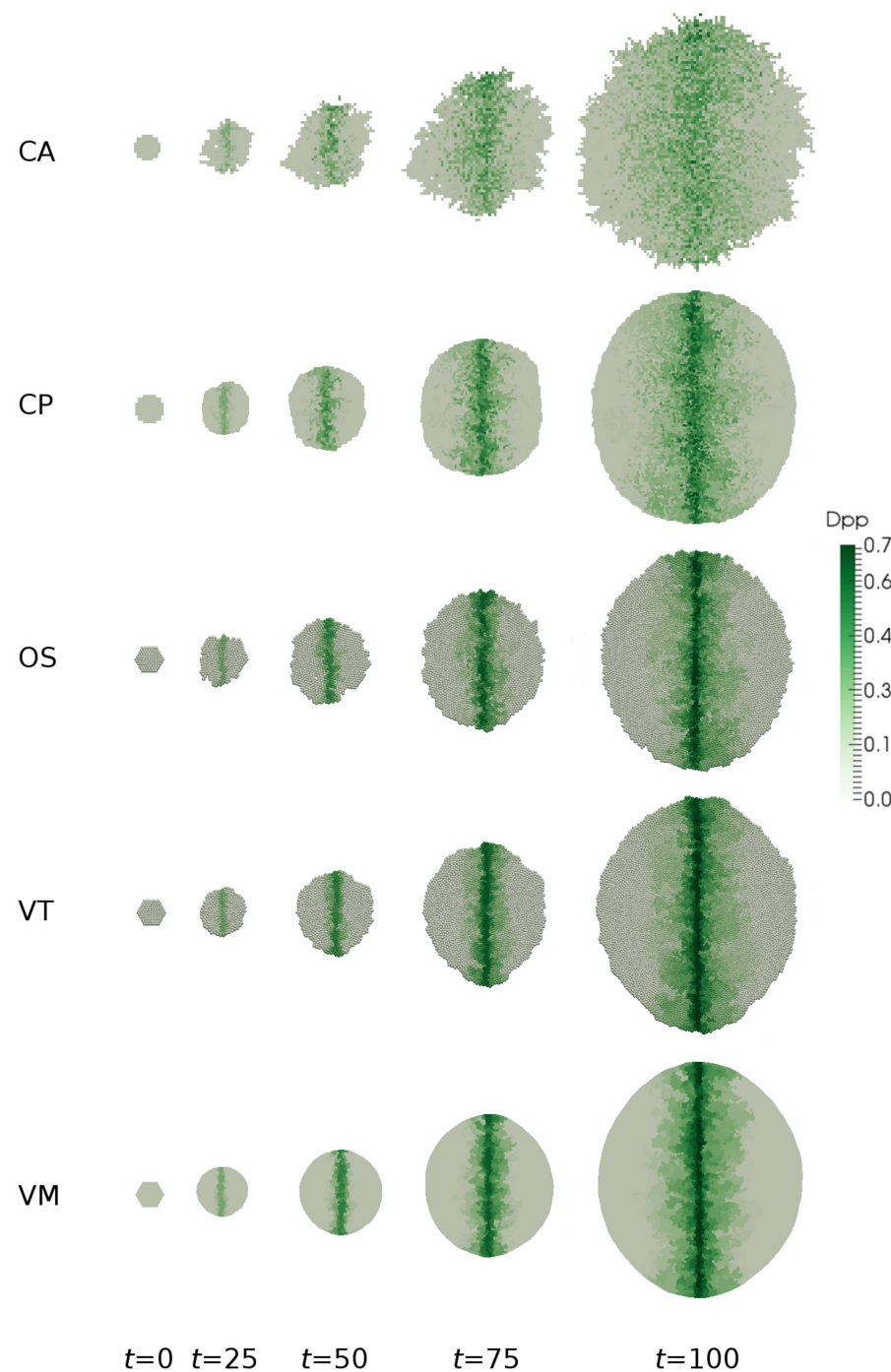


**Fig 10. Simulations of morphogen-dependent proliferation.** Snapshots of the tissue and associated morphogen distribution are shown at selected times for each model. Parameter values are given in Tables 1 and 5. A video of these simulations is given in [S4 Movie](#).

doi:10.1371/journal.pcbi.1005387.g010

precedence over qualitative comparison. In this context, we must investigate if the model framework chosen might amplify or diminish the effects of certain processes. To this end, the present work seeks to advance our comparative understanding of different classes of models in the context of cell and tissue biology.

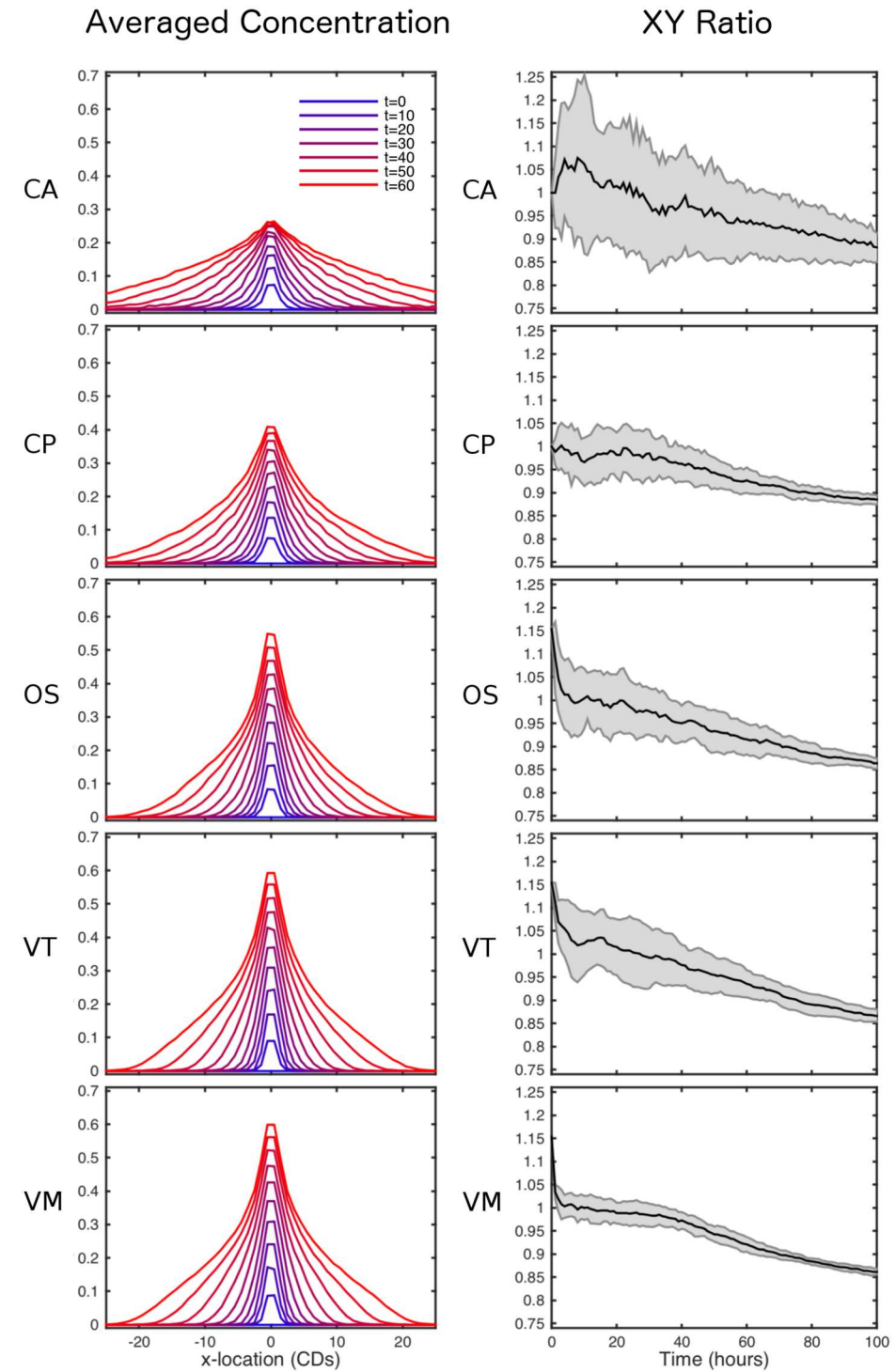


**Fig 11. Comparison of spatio-temporal morphogen and tissue shape dynamics across simulations.**

Left: the morphogen distribution is plotted at selected times as an average over the  $x$  direction and over 20 simulations. Results are shown for each model: CA; CP; OS; VT; and VM. Right: as a measure of tissue anisotropy, the ratio of the widths of the tissue in the  $x$  and  $y$  directions is computed as a function of time for each model. For each model, we plot the mean and standard error of this ratio across 20 simulations. Parameter values are given in Tables 1 and 5.

doi:10.1371/journal.pcbi.1005387.g011

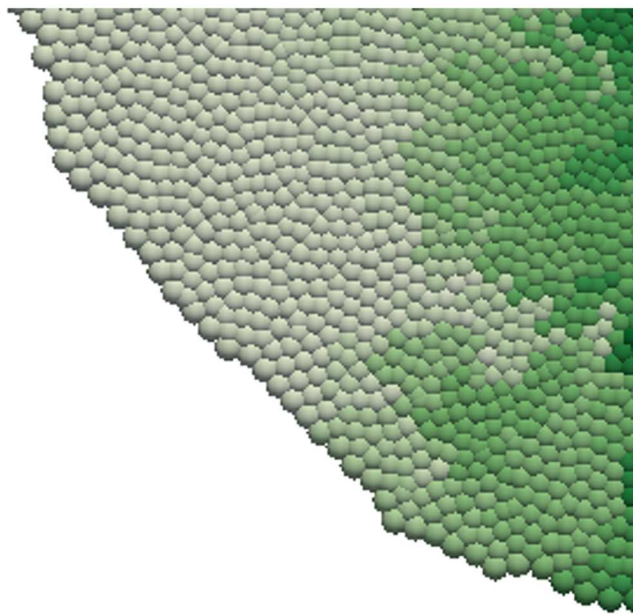


**Fig 12. Illustration of edge artefact in VT simulations on growing domains.** Closeup of bottom right of the  $t=100$  snapshot from the VT model in [Fig 10](#).

doi:10.1371/journal.pcbi.1005387.g012

A variety of cell-based approaches have been developed over the last few years. These models range from lattice-based cellular automata to lattice-free models that treat cells as point-like particles or extended shapes. Such models have proven useful in gaining mechanistic insight into the coordinated behaviour of populations of cells in tissues. However, it remains difficult to accurately compare between different modelling approaches, since one cannot distinguish between differences in behaviour due to the underlying model assumptions and those due to differences in the numerical implementation. Here, we have exploited the availability of an implementation of five popular cell-based modelling approaches within a consistent computational framework, Chaste. This framework allows one to easily change constitutive assumptions within these models. In each case we have provided full details of all technical aspects of our model implementations. An important finding of this study is that, with variable levels of success, it is possible to use each model investigated to represent the various behaviours of interest. Moreover, even though individual simulations may have visual differences, the bulk properties of the simulations were comparable in almost every case. However, there were differences (detailed below) and these could influence biological conclusions being drawn from the simulations.

We compared model implementations using four case studies, chosen to reflect the key cellular processes of proliferation, adhesion, and short- and long-range signalling. These case studies demonstrate the applicability of each model and provide a guide for model usage. While on a qualitative level each model exhibited similar behaviour, this was mainly achieved through parameter choice and fitting. Parameters were chosen to give consistent behaviour where possible. When choosing which model to use, one should bear in mind the following.

Certain case studies presented in this study are more aligned with particular models. For instance, in the adhesion example the CP and VM models are designed to explicitly represent cell sorting (through cell boundary energy terms) whereas the other models needed modification to represent the same phenomena. In fact, in the OS and VT (and to some extent the VM) models, the ability to sort completely was limited by the presence of local energy minima and a

noise component of cell motion was required to mitigate this. However, as the level of noise was increased, artefacts can be introduced into the models, for example the tessellation may become non-conformal leading to voids in the tissue.

The implementation of other features, such as boundary conditions, can also influence simulation outcomes. This was observed in the proliferation example where the rate of neutral drift was significantly different in the VM compared to the other models, due to additional adhesion of cells to the bottom of the domain. In this study we did not implement contact inhibition for the CA model as our definitions of contact inhibition required cells to be different sizes. It is possible to implement an alternative form of contact inhibition in the CA model by restricting division events to only occur when there is sufficient free space [64]; however, this would again result in a different behaviour to our simulations.

A key difference between the models we considered lies in the definition of cell connectivity. It is possible for cells in the same configuration to have different neighbours under different models. For example, when under compression, cells in the OS model can have more neighbours than similarly sized cells in the CP, VT or VM models. The effects of this can be seen in the short-range signalling example with a high degree of proliferation.

Finally, the models differ vastly on how long they take to simulate. In their original uncoupled forms, the least computationally complex model to simulate is the CA, followed in order by the CP, OS, VT and VM. However, this complexity depends on what is coupled to the models, at both the subcellular and tissue levels. Specifically, in order to make the CP model equivalent to the other models when coupling to subcellular and tissue level processes, we have chosen to use a time step that is smaller than that typically used in CP simulations, increasing the computation time.

In the following we compare the computational times for each case study as measured from our implementation of the different models in Chaste. To illustrate relative computation times, we record in [Table 6](#) the run time for a typical simulation of each case study, across the five models considered. We emphasise that these times are heavily dependent on the implementation of each model within Chaste, which is more heavily optimised for off-lattice models. In particular, the computation time for the CP model is likely to be significantly reduced if other software implementations of this class of model are used [65], [66]. We see that (except for the CP model) the level of computational time is roughly as expected, increasing with complexity with the OS and VT models being similar. There are exceptions to this. For example, the CA and CP simulations of the long-range signalling example take longer than may be expected. This is due to the method used to calculate the growing PDE mesh in our computational implementation in Chaste, which is optimal for off-lattice models; future work will involve developing optimised numerical techniques that exploit the lattice structure of the on-lattice models. On the other hand, the VM simulation of the proliferation example is quicker than may be expected; this is due to the choice of parameters leading to there being slightly fewer cells in the VM simulation for this example, reducing the computational demands.

Parallelisation is one way to both decrease computational time and to also be able to solve larger problems. Of the models considered, the CA model is simplest to parallelise. While

**Table 6. Approximate simulation times.** Run time (in seconds, on a single core of an Intel i7 processor) for typical single runs for each case study.

Example	CA	CP	OS	VT	VM
Adhesion	34	1638	168	625	321
Proliferation	44	4336	1218	2752	2419
Short-range signalling	166	7536	2837	4433	9983
Long-range signalling	1393	23741	804	789	5803

doi:10.1371/journal.pcbi.1005387.t006

**Table 7. Appropriate models.** Level of appropriateness of model: **highly appropriate**—model was developed in order to investigate this mechanism; **appropriate**—model can be used for this mechanism with minimal effort; **less appropriate**—model can only be used with this mechanism through careful tuning of parameters to match more appropriate models. Where appropriate advantages and disadvantages of each model in each example are given.

Example	CA	CP	OS	VT	VM
Adhesion	<b>Appropriate:</b> required Potts-like extension for differential adhesion	<b>Highly appropriate:</b> this is the model problem for the CP model	<b>Less appropriate:</b> unnatural differential adhesion, no engulfment	<b>Less appropriate:</b> unnatural differential adhesion, no engulfment	<b>Highly appropriate:</b> a model problem for the VM
Proliferation	<b>Less appropriate:</b> no cell compression	<b>Appropriate:</b> motility parameters tuned for stability	<b>Highly appropriate:</b> similarities to the VT model give same advantages	<b>Highly appropriate:</b> established paradigm for crypt models, previously fit to data	<b>Appropriate:</b> boundary conditions influence natural drift
Short-range signalling	<b>Less appropriate:</b> lattice artifacts, instantaneous neighbour transition	<b>Less appropriate:</b> lattice artifacts, excessive stochasticity with chosen parameters (required for mechanical stability)	<b>Highly appropriate:</b> smooth neighbour transition, copes with high levels of compression	<b>Highly appropriate:</b> smooth neighbour transition, copes with high levels of compression	<b>Appropriate:</b> parameter choice to prevent inverted elements from hyper proliferation
Long-range signalling	<b>Less appropriate:</b> costs for calculating FE mesh, lattice artifacts, extra transport of morphogen with movement	<b>Appropriate:</b> costs for calculating FE mesh	<b>Appropriate:</b> costs for calculating FE mesh	<b>Highly appropriate:</b> ready built FE mesh with 1-1 correspondence between cells and nodes	<b>Highly appropriate:</b> FE mesh generation from cells, FE mesh more refined than cells

doi:10.1371/journal.pcbi.1005387.t007

more advanced, the CP model has been parallelised in publicly available software packages [65], as has the OS model [67]. In the VT and VM cases, the implementations are much more involved. These considerations are summarised in Table 7.

The present study provides a starting point for a number of further avenues for research. First, there remains a need for theoretical and computational tools with which to easily perform quantitative model comparisons. Our results indicate that for many of the sorts of questions these types of model are currently being used to address, there is likely to be little difference in model predictions. However, such models are nevertheless moving toward a more quantitative footing, particularly as the resolution of experimental data at the cell to tissue scale improves. Further progress in this area will be accelerated by advances in automating the process of model specification and implementation, for example through extended use of mark-up languages such as SBML, FieldML and MultiCellDS.

Here we have made use of a consistent simulation framework, Chaste, within which to compare different classes of cell-based model. A longer-term challenge is to extend such comparison studies across simulation tools, of which there is an increasing ecosystem, including CompuCell3d [65], Morpheus [66], EPISIM [68], CellSys [69], VirtualLeaf [70], Biocellion [71], BioFVM [72], LBIBCell [73] and EmbryoMaker [74]. We emphasize here the lack of ‘benchmarks’ on which to make such comparisons. We propose that the present study offers four examples that could offer such benchmarks. Since some modelling paradigms are capable of reproducing certain biological phenomena and others are not, there is no benchmark on which all models will produce the same result; here, by selecting several simple biologically-inspired test cases we have gone some way to narrowing down the search for suitable benchmarks.

Throughout this study we have concentrated on 2D studies. However, many of the models considered have also been implemented in three dimensions both in previous studies and in the Chaste modelling framework, for example in the case of overlapping spheres models of the intestinal crypt [42], [75] or 3D vertex models of the mouse blastocyst [76]. Of the models considered in the present study, vertex models are arguably the most technically challenging to

extend to three dimensions, due to the complexity of the possible cell rearrangements and force calculations.

Work has also been done to model individual cells at a finer resolution by considering them to be composed of mesoscopic volume elements, which enables cell geometry and mechanical response to be emergent, rather than imposed, properties. These include the subcellular element model [77], which may be thought of as a natural extension of the cell centre model, and the finite element model [13] and immersed boundary model [14], which use alternative approaches to decompose cell shapes into volumetric or surface elements in a much more detailed manner than the cell-based models considered in this study.

## Supporting information

### S1 Movie. Video of simulations of cell sorting due to differential adhesion, from Fig 2.

Cells of type A and B are shown in purple and green, respectively. Engulfment of type-B cells occurs most readily in the CA, CP and VM models. Parameter values are given in Tables 1 and 2.

S1\_Movie.mp4 or [https://youtu.be/4YZp\\_WmBZTI](https://youtu.be/4YZp_WmBZTI).  
(MP4)

### S2 Movie. Video of simulations of monoclonal conversion in the colonic crypt, from Fig 5.

In each simulation at time  $t = 0$ , every cell is regarded as a clonal population and given a different colour, which is inherited by its progeny. These populations evolve in time due to cell proliferation and sloughing from the crypt orifice, resulting in a single clone eventually taking over the entire crypt. Parameter values are given in Tables 1 and 3, with  $r_{CI} = 0.8$ .

S2\_Movie.mp4 or <https://youtu.be/F04IIE2PyY0>.  
(MP4)

### S3 Movie. Video of simulations of lateral inhibition in a proliferating tissue, from Fig 8.

Parameter values are given in Tables 1 and 4 with  $p_{div} = 0.1$ .

S3\_Movie.mp4 or <https://youtu.be/SX2GFOr0Dus>.  
(MP4)

### S4 Movie. Video of simulations of morphogen-dependent proliferation, from Fig 10.

Parameter values are given in Tables 1 and 5.

S4\_Movie.mp4 or <https://youtu.be/Yl2GT2x2ohc>.  
(MP4)

## Acknowledgments

The authors acknowledge the contributions made by Fergus Cooper, Jonathan Cooper, James Grogan, Daniel Harvey, Jochen Kursawe and Martin Robinson to development of the cell-based component of the Chaste software library (<http://www.cs.ox.ac.uk/chaste>). The authors would like to thank Walter de Back for his constructive feedback on the manuscript.

## Author Contributions

**Conceptualization:** JMO AGF.

**Data curation:** JMO AGF JMPF.

**Formal analysis:** JMO AGF.

**Funding acquisition:** PKM DJG.

**Investigation:** JMO AGF.

**Methodology:** JMO AGF.

**Project administration:** JMO AGF.

**Resources:** PKM DJG.

**Software:** JMO AGF JMPF.

**Supervision:** PKM DJG.

**Validation:** JMO AGF JMPF.

**Visualization:** JMO AGF JMPF.

**Writing – original draft:** JMO AGF.

**Writing – review & editing:** JMO AGF JMPF PKM DJG.

## References

1. Lee Y, Kouvroukoglou S, McIntire LV, Zygourakis K. A cellular automaton model for the proliferation of migrating contact-inhibited cells. *Biophys J.* 1995; 69:1284. doi: [10.1016/S0006-3495\(95\)79996-9](https://doi.org/10.1016/S0006-3495(95)79996-9) PMID: [8534799](https://pubmed.ncbi.nlm.nih.gov/8534799/)
2. Block M, Schöll E, Drasdo D. Classifying the expansion kinetics and critical surface dynamics of growing cell populations. *Phys Rev Lett.* 2007; 99:248101. doi: [10.1103/PhysRevLett.99.248101](https://doi.org/10.1103/PhysRevLett.99.248101) PMID: [18233492](https://pubmed.ncbi.nlm.nih.gov/18233492/)
3. Graner F, Glazier JA. Simulation of biological cell sorting using a two-dimensional extended Potts model. *Phys Rev Lett.* 1992; 69:2013. doi: [10.1103/PhysRevLett.69.2013](https://doi.org/10.1103/PhysRevLett.69.2013) PMID: [10046374](https://pubmed.ncbi.nlm.nih.gov/10046374/)
4. Glazier JA, Graner F. Simulation of the differential adhesion driven rearrangement of biological cells. *Phys Rev E.* 1993; 47:2128–2154. doi: [10.1103/PhysRevE.47.2128](https://doi.org/10.1103/PhysRevE.47.2128)
5. Izaguirre JA, Chaturvedi R, Huang C, Cickovski T, Coffland J, Thomas G, et al. CompuCell, a multi-model framework for simulation of morphogenesis. *Bioinformatics.* 2004; 20:1129–1137. doi: [10.1093/bioinformatics/bth050](https://doi.org/10.1093/bioinformatics/bth050) PMID: [14764549](https://pubmed.ncbi.nlm.nih.gov/14764549/)
6. Shirinifard A, Gens JS, Zaitlen BL, Poplawski NJ, Swat M, Glazier JA. 3D multi-cell simulation of tumor growth and angiogenesis. *PLOS ONE.* 2009; 4:e7190. doi: [10.1371/journal.pone.0007190](https://doi.org/10.1371/journal.pone.0007190) PMID: [19834621](https://pubmed.ncbi.nlm.nih.gov/19834621/)
7. Drasdo D, Höhme S. A single-cell-based model of tumor growth *in vitro*: monolayers and spheroids. *Phys Biol.* 2005; 2:133. doi: [10.1088/1478-3975/2/3/001](https://doi.org/10.1088/1478-3975/2/3/001) PMID: [16224119](https://pubmed.ncbi.nlm.nih.gov/16224119/)
8. Meineke FA, Potten CS, Loeffler M. Cell migration and organization in the intestinal crypt using a lattice-free model. *Cell Prolif.* 2001; 34:253–266. doi: [10.1046/j.0960-7722.2001.00216.x](https://doi.org/10.1046/j.0960-7722.2001.00216.x) PMID: [11299883](https://pubmed.ncbi.nlm.nih.gov/11299883/)
9. Schaller G, Meyer-Hermann M. Kinetic and dynamic Delaunay tetrahedralizations in three dimensions. *Comput Phys Commun.* 2004; 162:9–23. doi: [10.1016/j.cpc.2004.06.066](https://doi.org/10.1016/j.cpc.2004.06.066)
10. De Matteis G, Graudenzi A, Antoniotti M. A review of spatial computational models for multi-cellular systems, with regard to intestinal crypts and colorectal cancer development. *J Math Biol.* 2013; 66 (7):1409–1462. doi: [10.1007/s00285-012-0539-4](https://doi.org/10.1007/s00285-012-0539-4) PMID: [22565629](https://pubmed.ncbi.nlm.nih.gov/22565629/)
11. Galle J, Hoffmann M, Aust G. From single cells to tissue architecture—a bottom-up approach to modelling the spatio-temporal organisation of complex multi-cellular systems. *J Math Biol.* 2009; 58(1–2):261–283. doi: [10.1007/s00285-008-0172-4](https://doi.org/10.1007/s00285-008-0172-4) PMID: [18386011](https://pubmed.ncbi.nlm.nih.gov/18386011/)
12. Jones GW, Chapman SJ. Modeling growth in biological materials. *SIAM Review.* 2012; 54(1):52–118. doi: [10.1137/080731785](https://doi.org/10.1137/080731785)
13. Brodland GW, Chen HH. The mechanics of cell sorting and envelopment. *J Biomech.* 2000; 33:845–851.
14. Rejniak KA. An immersed boundary framework for modelling the growth of individual cells: an application to the early tumour development. *J Theor Biol.* 2007; 247:186–204. doi: [10.1016/j.jtbi.2007.02.019](https://doi.org/10.1016/j.jtbi.2007.02.019) PMID: [17416390](https://pubmed.ncbi.nlm.nih.gov/17416390/)
15. Sandersius SA, Newman TJ. Modeling cell rheology with the Subcellular Element Model. *Phys Biol.* 2008; 5:015002. doi: [10.1088/1478-3975/5/1/015002](https://doi.org/10.1088/1478-3975/5/1/015002) PMID: [18403827](https://pubmed.ncbi.nlm.nih.gov/18403827/)

16. Walker DC, Southgate J. The virtual cell—a candidate co-ordinator for ‘middle-out’ modelling of biological systems. *Briefings in Bioinformatics*. 2009; p. bbp010. doi: [10.1093/bib/bbp010](https://doi.org/10.1093/bib/bbp010) PMID: [19293250](https://pubmed.ncbi.nlm.nih.gov/19293250/)
17. Aegerter-Wilmsen T, Smith AC, Christen AJ, Aegerter CM, Hafen E, Basler K. Exploring the effects of mechanical feedback on epithelial topology. *Development*. 2010; 137:499–506. doi: [10.1242/dev.041731](https://doi.org/10.1242/dev.041731) PMID: [20081194](https://pubmed.ncbi.nlm.nih.gov/20081194/)
18. Schilling S, Willecke M, Aegerter-Wilmsen T, Cirpka OA, Basler K, von Mering C. Cell-sorting at the A/P boundary in the *Drosophila* wing primordium: a computational model to consolidate observed non-local effects of Hh signaling. *PLoS Comput Biol*. 2011; 7:e1002025. doi: [10.1371/journal.pcbi.1002025](https://doi.org/10.1371/journal.pcbi.1002025) PMID: [21490725](https://pubmed.ncbi.nlm.nih.gov/21490725/)
19. Smith AM, Baker RE, Kay D, Maini PK. Incorporating chemical signalling factors into cell-based models of growing epithelial tissues. *J Math Biol*. 2011; 65:441–463. doi: [10.1007/s00285-011-0464-y](https://doi.org/10.1007/s00285-011-0464-y) PMID: [21898111](https://pubmed.ncbi.nlm.nih.gov/21898111/)
20. Salbreux G, Barthel LK, Raymond PA, Lubensky DK. Coupling mechanical deformations and planar cell polarity to create regular patterns in the zebrafish retina. *PLoS Comput Biol*. 2012; 8:e1002618. doi: [10.1371/journal.pcbi.1002618](https://doi.org/10.1371/journal.pcbi.1002618) PMID: [22936893](https://pubmed.ncbi.nlm.nih.gov/22936893/)
21. Hester SD, Belmonte JM, Gens JS, Clendenon SG, Glazier JA. A multi-cell, multi-scale model of vertebrate segmentation and somite formation. *PLoS Comput Biol*. 2011; 7:e1002155. doi: [10.1371/journal.pcbi.1002155](https://doi.org/10.1371/journal.pcbi.1002155) PMID: [21998560](https://pubmed.ncbi.nlm.nih.gov/21998560/)
22. Anderson ARA, Weaver AM, Cummings PT, Quaranta V. Tumor morphology and phenotypic evolution driven by selective pressure from the microenvironment. *Cell*. 2006; 127:905–915. doi: [10.1016/j.cell.2006.09.042](https://doi.org/10.1016/j.cell.2006.09.042) PMID: [17129778](https://pubmed.ncbi.nlm.nih.gov/17129778/)
23. Pitt-Francis J, Pathmanathan P, Bernabeu MO, Bordas R, Cooper J, Fletcher AG, et al. Chaste: a test-driven approach to software development for biological modelling. *Comput Phys Commun*. 2009; 180:2452–2471.
24. Mirams GR, Arthurs CJ, Bernabeu MO, Bordas R, Cooper J, Corrias A, et al. Chaste: an open source C ++ library for computational physiology and biology. *PLoS Comput Biol*. 2013; 9:e1002970. doi: [10.1371/journal.pcbi.1002970](https://doi.org/10.1371/journal.pcbi.1002970) PMID: [23516352](https://pubmed.ncbi.nlm.nih.gov/23516352/)
25. Yates CA, Parker A, Baker RE. Incorporating pushing in exclusion-process models of cell migration. *Phys Rev E*. 2015; 91:052711. doi: [10.1103/PhysRevE.91.052711](https://doi.org/10.1103/PhysRevE.91.052711)
26. Deutsch A, Dormann S. Cellular automaton modeling of biological pattern formation: characterization, applications, and analysis. Springer Science & Business Media; 2007.
27. Durand M, Guesnet E. An efficient Cellular Potts Model algorithm that forbids cell fragmentation. *Comput Phys Commun*. 2016;
28. Purcell EM. Life at low Reynolds number. *Am J Phys*. 1977; 45:3–11. doi: [10.1119/1.10903](https://doi.org/10.1119/1.10903)
29. Atwell K, Qin Z, Gavaghan D, Kugler H, Hubbard EJA, Osborne JM. Mechano-logical model of *C. elegans* germ line suggests feedback on the cell cycle. *Development*. 2015; 142:3902–3911. doi: [10.1242/dev.126359](https://doi.org/10.1242/dev.126359) PMID: [26428008](https://pubmed.ncbi.nlm.nih.gov/26428008/)
30. Pathmanathan P, Cooper J, Fletcher A, Mirams G, Murray P, Osborne J, et al. A computational study of discrete mechanical tissue models. *Phys Biol*. 2009; 6:036001. doi: [10.1088/1478-3975/6/3/036001](https://doi.org/10.1088/1478-3975/6/3/036001) PMID: [19369704](https://pubmed.ncbi.nlm.nih.gov/19369704/)
31. van Leeuwen IMM, Mirams GR, Walter A, Fletcher AG, Murray P, Osborne J, et al. An integrative computational model for intestinal tissue renewal. *Cell Prolif*. 2009; 42:617–636. doi: [10.1111/j.1365-2184.2009.00627.x](https://doi.org/10.1111/j.1365-2184.2009.00627.x) PMID: [19622103](https://pubmed.ncbi.nlm.nih.gov/19622103/)
32. Farhadifar R, Röper JC, Aigouy B, Eaton S, Jülicher F. The influence of cell mechanics, cell-cell interactions, and proliferation on epithelial packing. *Curr Biol*. 2007; 17:2095–2104. doi: [10.1016/j.cub.2007.11.049](https://doi.org/10.1016/j.cub.2007.11.049) PMID: [18082406](https://pubmed.ncbi.nlm.nih.gov/18082406/)
33. Fletcher AG, Osterfield M, Baker RE, Shvartsman SY. Vertex models of epithelial morphogenesis. *Bioophys J*. 2014; 106:2291–2304. doi: [10.1016/j.bpj.2013.11.4498](https://doi.org/10.1016/j.bpj.2013.11.4498) PMID: [24896108](https://pubmed.ncbi.nlm.nih.gov/24896108/)
34. Kursawe J, Brodskiy PA, Zartman JJ, Baker RE, Fletcher AG. Capabilities and limitations of tissue size control through passive mechanical forces. *PLoS Comput Biol*. 2015; 11:e1004679. doi: [10.1371/journal.pcbi.1004679](https://doi.org/10.1371/journal.pcbi.1004679) PMID: [26713738](https://pubmed.ncbi.nlm.nih.gov/26713738/)
35. Fletcher AG, Osborne JM, Maini PK, Gavaghan DJ. Implementing vertex dynamics models of cell populations in biology within a consistent computational framework. *Prog Biophys Mol Biol*. 2013; 113:299–326. doi: [10.1016/j.pbiomolbio.2013.09.003](https://doi.org/10.1016/j.pbiomolbio.2013.09.003) PMID: [24120733](https://pubmed.ncbi.nlm.nih.gov/24120733/)
36. Weliky M, Oster G. The mechanical basis of cell rearrangement. I. Epithelial morphogenesis during Fundulus epiboly. *Development*. 1990; 109:373–386. PMID: [2401201](https://pubmed.ncbi.nlm.nih.gov/2401201/)
37. Osborne JM. Multiscale model of colorectal cancer using the cellular Potts framework. *Cancer Inform*. 2015; 14:83. doi: [10.4137/CIN.S19332](https://doi.org/10.4137/CIN.S19332) PMID: [26461973](https://pubmed.ncbi.nlm.nih.gov/26461973/)

38. Steinberg MS. Does differential adhesion govern self-assembly processes in histogenesis? Equilibrium configurations and the emergence of a hierarchy among populations of embryonic cells. *J Exp Zool.* 1970; 173:395–433. doi: [10.1002/jez.1401730406](https://doi.org/10.1002/jez.1401730406) PMID: [5429514](https://pubmed.ncbi.nlm.nih.gov/5429514/)
39. Harris AK. Is cell sorting caused by differences in the work of intercellular adhesion? A critique of the Steinberg hypothesis. *J Theor Biol.* 1976; 61:267–285. doi: [10.1016/0022-5193\(76\)90019-9](https://doi.org/10.1016/0022-5193(76)90019-9) PMID: [985668](https://pubmed.ncbi.nlm.nih.gov/985668/)
40. Brodland GW. Computational modeling of cell sorting, tissue engulfment, and related phenomena: A review. *Appl Mech Rev.* 2004; 57:47–77. doi: [10.1115/1.1583758](https://doi.org/10.1115/1.1583758)
41. Dunn SJ, Nähthke IS, Osborne JM. Computational models reveal a passive mechanism for cell migration in the crypt. *PLOS ONE.* 2013; 8(11):e80516. doi: [10.1371/journal.pone.0080516](https://doi.org/10.1371/journal.pone.0080516) PMID: [24260407](https://pubmed.ncbi.nlm.nih.gov/24260407/)
42. Dunn SJ, Osborne JM, Appleton PL, Nähthke I. Combined changes in Wnt signaling response and contact inhibition induce altered proliferation in radiation-treated intestinal crypts. *Mol Biol Cell.* 2016; 27(11):1863–1874. doi: [10.1091/mbc.E15-12-0854](https://doi.org/10.1091/mbc.E15-12-0854) PMID: [27053661](https://pubmed.ncbi.nlm.nih.gov/27053661/)
43. Dietrich C, Scherwat J, Faust D, Oesch F. Subcellular localization of  $\beta$ -catenin is regulated by cell density. *Biochem Biophys Res Commun.* 2002; 292:195–199. doi: [10.1006/bbrc.2002.6625](https://doi.org/10.1006/bbrc.2002.6625) PMID: [11890692](https://pubmed.ncbi.nlm.nih.gov/11890692/)
44. Avvisato CL, Yang X, Shah S, Hoxter B, Li W, Gaynor R, et al. Mechanical force modulates global gene expression and  $\beta$ -catenin signaling in colon cancer cells. *J Cell Sci.* 2007; 120(15):2672–2682. doi: [10.1242/jcs.03476](https://doi.org/10.1242/jcs.03476) PMID: [17635998](https://pubmed.ncbi.nlm.nih.gov/17635998/)
45. Whitehead J, Vignjevic D, Fütterer C, Beaurepaire E, Robine S, Farge E. Mechanical factors activate  $\beta$ -catenin-dependent oncogene expression in APC $^{1638N^+}$  mouse colon. *HFSP J.* 2008; 2(5):286–294. doi: [10.2976/1.2955566](https://doi.org/10.2976/1.2955566) PMID: [19404440](https://pubmed.ncbi.nlm.nih.gov/19404440/)
46. Fletcher AG, Murray PJ, Maini PK. Multiscale modelling of intestinal crypt organization and carcinogenesis. *Math Mod Meth Appl Sci.* 2015; 25:2563–2585. doi: [10.1142/S0218202515400187](https://doi.org/10.1142/S0218202515400187)
47. Lloyd-Lewis B, Fletcher AG, Dale TC, Byrne HM. Toward a quantitative understanding of the Wnt/ $\beta$ -catenin pathway through simulation and experiment. *WIREs Syst Biol Med.* 2013; 5:391–407.
48. Drasdo D, Höhme S. Individual-based approaches to birth and death in avascular tumors. *Math Comput Model.* 2003; 37:1163–1175.
49. Drasdo D, Höhme S, Block M. On the role of physics in the growth and pattern formation of multi-cellular systems: What can we learn from individual-cell based models? *J Stat Phys.* 2007; 128:287–345. doi: [10.1007/s10955-007-9289-x](https://doi.org/10.1007/s10955-007-9289-x)
50. Galle J, Loeffler M, Drasdo D. Modeling the effect of deregulated proliferation and apoptosis on the growth dynamics of epithelial cell populations *in vitro*. *Biophys J.* 2005; 88:62–75. doi: [10.1529/biophysj.104.041459](https://doi.org/10.1529/biophysj.104.041459) PMID: [15475585](https://pubmed.ncbi.nlm.nih.gov/15475585/)
51. Osborne JM, Walter A, Kershaw SK, Mirams GR, Fletcher AG, Pathmanathan P, et al. A hybrid approach to multi-scale modelling of cancer. *Phil Trans R Soc A.* 2010; 368:5013–5028. doi: [10.1098/rsta.2010.0173](https://doi.org/10.1098/rsta.2010.0173) PMID: [20921009](https://pubmed.ncbi.nlm.nih.gov/20921009/)
52. Mirams GR, Fletcher AG, Maini PK, Byrne HM. A theoretical investigation of the effect of proliferation and adhesion on monoclonal conversion in the colonic crypt. *J Theor Biol.* 2012; 312:143–156. doi: [10.1016/j.jtbi.2012.08.002](https://doi.org/10.1016/j.jtbi.2012.08.002) PMID: [22902425](https://pubmed.ncbi.nlm.nih.gov/22902425/)
53. Leontieva OV, Demidenko ZN, Blagosklonny MV. Contact inhibition and high cell density deactivate the mammalian target of rapamycin pathway, thus suppressing the senescence program. *Proc Natl Acad Sci USA.* 2014; 111:8832–8837. doi: [10.1073/pnas.1405723111](https://doi.org/10.1073/pnas.1405723111) PMID: [24889617](https://pubmed.ncbi.nlm.nih.gov/24889617/)
54. Artavanis-Tsakonas S, Rand MD, Lake RJ. Notch signaling: cell fate control and signal integration in development. *Science.* 1999; 284:770–776. doi: [10.1126/science.284.5415.770](https://doi.org/10.1126/science.284.5415.770) PMID: [10221902](https://pubmed.ncbi.nlm.nih.gov/10221902/)
55. Collier JR, Monk NAM, Maini PK, Lewis JH. Pattern formation by lateral inhibition with feedback: a mathematical model of delta-notch intercellular signalling. *J Theor Biol.* 1996; 183:429–446. doi: [10.1006/jtbi.1996.0233](https://doi.org/10.1006/jtbi.1996.0233) PMID: [9015458](https://pubmed.ncbi.nlm.nih.gov/9015458/)
56. Podgorski GJ, Bansal M, Flann NS. Regular mosaic pattern development: a study of the interplay between lateral inhibition, apoptosis and differential adhesion. *Theor Biol Med Model.* 2007; 4(1):1.
57. Cohen M, Baum B, Miodownik M. The importance of structured noise in the generation of self-organizing tissue patterns through contact-mediated cell-cell signalling. *J R Soc Interface.* 2011; 8(59):787–798. doi: [10.1098/rsif.2010.0488](https://doi.org/10.1098/rsif.2010.0488) PMID: [21084342](https://pubmed.ncbi.nlm.nih.gov/21084342/)
58. Owen MR, Sherratt JA. Mathematical modelling of juxtacrine cell signalling. *Math Biosci.* 1998; 153:125–150.
59. Wearing HJ, Sherratt JA. Nonlinear analysis of juxtacrine patterns. *SIAM J Appl Math.* 2001; 62:283–309. doi: [10.1137/S003613990037220X](https://doi.org/10.1137/S003613990037220X)

60. Webb SD, Owen MR. Oscillations and patterns in spatially discrete models for developmental intercellular signalling. *J Math Biol.* 2004; 48:444–476. doi: [10.1007/s00285-003-0247-1](https://doi.org/10.1007/s00285-003-0247-1) PMID: [15052506](https://pubmed.ncbi.nlm.nih.gov/15052506/)
61. Wartlick O, Mumcu P, Jülicher F, Gonzalez-Gaitan M. Understanding morphogenetic growth control—lessons from flies. *Nat Rev Mol Cell Biol.* 2011; 12:594–604. doi: [10.1038/nrm3169](https://doi.org/10.1038/nrm3169) PMID: [21850035](https://pubmed.ncbi.nlm.nih.gov/21850035/)
62. Aegerter-Wilmsen T, Aegerter CM, Hafen E, Basler K. Model for the regulation of size in the wing imaginal disc of *Drosophila*. *Mech Dev.* 2007; 124:318–326. doi: [10.1016/j.mod.2006.12.005](https://doi.org/10.1016/j.mod.2006.12.005) PMID: [17293093](https://pubmed.ncbi.nlm.nih.gov/17293093/)
63. Mao Y, Tournier AL, Hoppe A, Kester L, Thompson BJ, Tapon N. Differential proliferation rates generate patterns of mechanical tension that orient tissue growth. *EMBO J.* 2013; 32(21):2790–2803. doi: [10.1038/embj.2013.197](https://doi.org/10.1038/embj.2013.197) PMID: [24022370](https://pubmed.ncbi.nlm.nih.gov/24022370/)
64. Simpson MJ, Merrifield A, Landman KA, Hughes BD. Simulating invasion with cellular automata: Connecting cell-scale and population-scale properties. *Phys Rev E.* 2007; 76:21918. doi: [10.1103/PhysRevE.76.021918](https://doi.org/10.1103/PhysRevE.76.021918)
65. Swat MH, Thomas GL, Belmonte JM, Shirinifard A, Hmeljak D, Glazier JA. Multi-scale modeling of tissues using CompuCell3D. *Methods Cell Biol.* 2012; 110:325. doi: [10.1016/B978-0-12-388403-9.00013-8](https://doi.org/10.1016/B978-0-12-388403-9.00013-8) PMID: [22482955](https://pubmed.ncbi.nlm.nih.gov/22482955/)
66. Starruß J, de Back W, Brusch L, Deutsch A. Morpheus: a user-friendly modeling environment for multi-scale and multicellular systems biology. *Bioinformatics.* 2014; 30(9):1331–1332. doi: [10.1093/bioinformatics/btt772](https://doi.org/10.1093/bioinformatics/btt772) PMID: [24443380](https://pubmed.ncbi.nlm.nih.gov/24443380/)
67. Harvey DG, Fletcher AG, Osborne JM, Pitt-Francis J. A parallel implementation of an off-lattice individual-based model of multicellular populations. *Comp Phys Comm.* 2015; 192:130–137.
68. Sütterlin T, Kolb C, Dickhaus H, Jäger D, Grabe N. Bridging the scales: semantic integration of quantitative SBML in graphical multi-cellular models and simulations with EPISIM and COPASI. *Bioinformatics.* 2013; 29(2):223–229. doi: [10.1093/bioinformatics/bts659](https://doi.org/10.1093/bioinformatics/bts659) PMID: [23162085](https://pubmed.ncbi.nlm.nih.gov/23162085/)
69. Hoehme S, Drasdo D. A cell-based simulation software for multi-cellular systems. *Bioinformatics.* 2010; 26(20):2641–2642. doi: [10.1093/bioinformatics/btq437](https://doi.org/10.1093/bioinformatics/btq437) PMID: [20709692](https://pubmed.ncbi.nlm.nih.gov/20709692/)
70. Merks RM, Guravage M, Inzé D, Beemster GT. VirtualLeaf: an open-source framework for cell-based modeling of plant tissue growth and development. *Plant Physiol.* 2011; 155(2):656–666. doi: [10.1101/pp.110.167619](https://doi.org/10.1101/pp.110.167619) PMID: [21148415](https://pubmed.ncbi.nlm.nih.gov/21148415/)
71. Kang S, Kahan S, McDermott J, Flann N, Shmulevich I. Biocellion: accelerating computer simulation of multicellular biological system models. *Bioinformatics.* 2014; 30(21):3101–3108. doi: [10.1093/bioinformatics/btu498](https://doi.org/10.1093/bioinformatics/btu498) PMID: [25064572](https://pubmed.ncbi.nlm.nih.gov/25064572/)
72. Ghaffarizadeh A, Friedman SH, Macklin P. BioFVM: an efficient, parallelized diffusive transport solver for 3-D biological simulations. *Bioinformatics.* 2016; 32(8):1256–1258. doi: [10.1093/bioinformatics/btv730](https://doi.org/10.1093/bioinformatics/btv730) PMID: [26656933](https://pubmed.ncbi.nlm.nih.gov/26656933/)
73. Tanaka S, Sichau D, Iber D. LBIBCell: a cell-based simulation environment for morphogenetic problems. *Bioinformatics.* 2015; 31(14):2340–2347. doi: [10.1093/bioinformatics/btv147](https://doi.org/10.1093/bioinformatics/btv147) PMID: [25770313](https://pubmed.ncbi.nlm.nih.gov/25770313/)
74. Marin-Riera M, Brun-Usan M, Zimm R, Välikangas T, et al. Computational modeling of development by epithelia, mesenchyme and their interactions: a unified model. *Bioinformatics.* 2016; 32(2):219–225. PMID: [26342230](https://pubmed.ncbi.nlm.nih.gov/26342230/)
75. Buske P, Galle J, Barker N, Aust G, Clevers H, Loeffler M. A comprehensive model of the spatio-temporal stem cell and tissue organisation in the intestinal crypt. *PLoS Comput Biol.* 2011; 7:e1001045. doi: [10.1371/journal.pcbi.1001045](https://doi.org/10.1371/journal.pcbi.1001045) PMID: [21253562](https://pubmed.ncbi.nlm.nih.gov/21253562/)
76. Honda H, Motosugi N, Nagai T, Tanemura M, Hiragi T. Computer simulation of emerging asymmetry in the mouse blastocyst. *Development.* 2008; 135:1407–1414. doi: [10.1242/dev.014555](https://doi.org/10.1242/dev.014555) PMID: [18359902](https://pubmed.ncbi.nlm.nih.gov/18359902/)
77. Newman TJ. Modeling multi-cellular systems using sub-cellular elements. *Math Biosci Eng.* 2005; 2:611–622.